Differential Proteome and Interactome Analysis Reveal the Basis of Pleiotropy Associated With the Histidine Methyltransferase Hpm1p

Authors

Tara K. Bartolec, Joshua J. Hamey, Andrew Keller, Juan D. Chavez, James E. Bruce, and Marc. R. Wilkins

Correspondence

m.wilkins@unsw.edu.au

Graphical Abstract

In Brief

The yeast histidine methyltransferase Hpm1p targets a ribosomal substrate but has many unexplained extraribosomal phenotypes. To understand these, we used protein expression analysis and quantitative cross-linking mass spectrometry to compare WT and Δhpm1 cells. This revealed a role of Hpm1p in metabolism, mitochondria, and membranes. Cross-linking mass spectrometry detected changes in protein structures and interactions and was a powerful means of understanding phenotype. Insights were different to those gained from expression analysis, making these techniques of great potential.
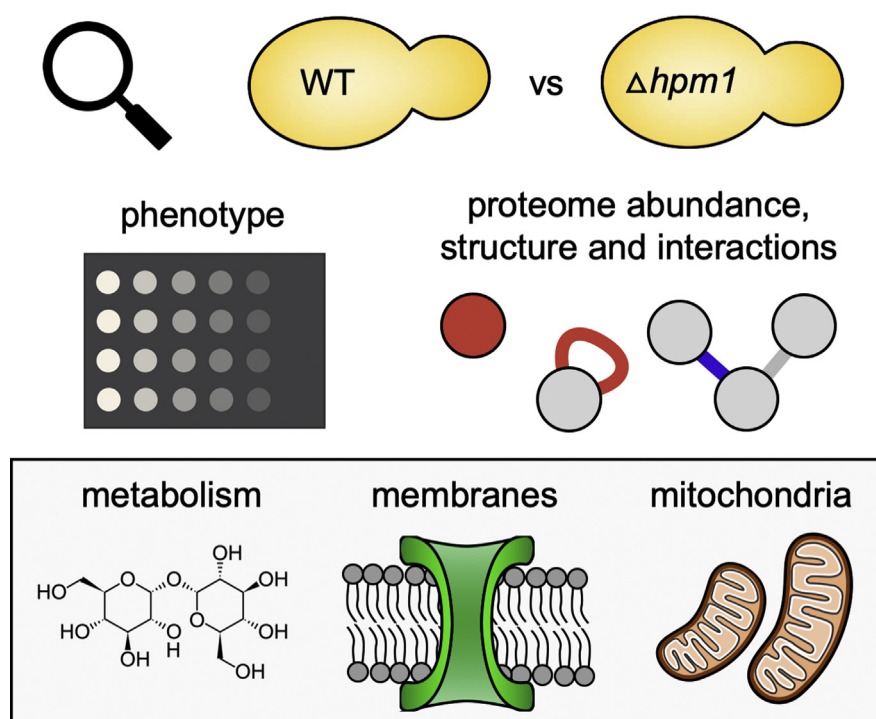
Highlights

- Novel extraribosomal functional phenotypes found on loss of Hpm1p.
- Large-scale *in vivo* quantitative and comparative crosslinking analysis performed.
- Changes detected in structures and interactions, independent of protein abundance.
- Phenotypes could be explained or predicted through crosslinking analysis.

https://doi.org/10.1016/j.mcpro.2022.100249

Differential Proteome and Interactome Analysis Reveal the Basis of Pleiotropy Associated With the Histidine Methyltransferase Hpm1p

Tara K. Bartolec[1] , **Joshua J. Hamey**[1], **Andrew Keller**[2], **Juan D. Chavez**[2] , **James E. Bruce**[2], and **Marc. R. Wilkins**[1,*]

The methylation of histidine is a post-translational modification whose function is poorly understood. Methyltransferase histidine protein methyltransferase 1 (Hpm1p) monomethylates H243 in the ribosomal protein Rpl3p and represents the only known histidine methyltransferase in *Saccharomyces cerevisiae*. Interestingly, the *hpm1* deletion strain is highly pleiotropic, with many extraribosomal phenotypes including improved growth rates in alternative carbon sources. Here, we investigate how the loss of histidine methyltransferase Hpm1p results in diverse phenotypes, through use of targeted mass spectrometry (MS), growth assays, quantitative proteomics, and differential crosslinking MS. We confirmed the localization and stoichiometry of the H243 methylation site, found unreported sensitivities of Δ*hpm1* yeast to nonribosomal stressors, and identified differentially abundant proteins upon *hpm1* knockout with clear links to the coordination of sugar metabolism. We adapted the emerging technique of quantitative large-scale stable isotope labeling of amino acids in cell culture crosslinking MS for yeast, which resulted in the identification of 1267 unique *in vivo* lysine–lysine crosslinks. By reproducibly monitoring over 350 of these in WT and Δ*hpm1*, we detected changes to protein structure or protein–protein interactions in the ribosome, membrane proteins, chromatin, and mitochondria. Importantly, these occurred independently of changes in protein abundance and could explain a number of phenotypes of Δ*hpm1*, not addressed by expression analysis. Further to this, some phenotypes were predicted solely from changes in protein structure or interactions and could be validated by orthogonal techniques. Taken together, these studies reveal a broad role for Hpm1p in yeast and illustrate how crosslinking MS will be an essential tool for understanding complex phenotypes.

Protein methylation is an important post-translational modification (PTM), which occurs predominantly on lysine and arginine residues in eukaryotic cells. Methylation of histidine residues (reviewed in Refs. (1, 2)) can also occur and was initially described for only a small number of proteins, including actin, myosin, myosin kinase, S100A9, the large subunit ribosomal protein L3, and more recently, a family of zinc transporter proteins (3, 4). The most well-studied example is the methylation of human β-actin H73, which has been shown to have important roles in regulating the stability of the actin cytoskeleton. The responsible methyltransferase SETD3 (5, 6) is implicated in a number of human diseases, including viral pathogenesis (7), liver tumorigenesis (8), and lymphoma (9), thus confirming the functional importance of histidine methylation. Because of the lack of available affinity reagents, our understanding of histidine methylation is less complete than that of lysine and arginine. However, a recent stringent reanalysis of ultra-deep human proteomic datasets has revealed that over 200 distinct proteins are histidine methylated (10), highlighting the need to improve our understanding of this unique PTM.

Histidine protein methyltransferase 1 (Hpm1p) was the first described histidine methyltransferase in any organism, and the only one known in the budding yeast *Saccharomyces cerevisiae* (11). It monomethylates the Tau nitrogen of histidine 243 (H243) in the large ribosomal subunit protein Rpl3p (uL3; universal large subunit ribosomal protein 3) to stoichiometric levels. Recent work has confirmed functional conservation of Hpm1p, with the human ortholog METTL18 (human methyltransferase-like protein 18) shown to methylate histidine 245 of human Rpl3 (12). In addition, orthologs exist in other eukaryotes including *Drosophila melanogaster*, *Caenorhabditis elegans*, and *Saccharomyces pombe* (11), suggesting that histidine methylation plays important roles across Eukarya. H243 is located in the buried tryptophan finger domain of yeast Rpl3p, which protrudes into the peptidyl transferase center of the assembled ribosome and makes extensive hydrogen-bonding contacts with the 25S rRNA. This finger is thought to function as a rocker, pushing

aminoacyl-tRNAs between the A-site (aminoacyl site of protein synthesis in the translating ribosome) and the P-site (peptidyl site of protein synthesis in the translating ribosome) (13, 14). Deletion of the *hpm1* (YIL110W) gene is nonlethal, but targeted studies of this strain have identified effects on ribosome assembly, fidelity, and structure. This is manifest in decreased 60S subunit synthesis, increased stop-codon readthrough, programmed −1 ribosomal frameshifting, amino acid misincorporation, and increased resistance to ribosome-binding drugs, such as cycloheximide and anisomycin (11, 15–17).

The *hpm1* deletion strain is highly pleiotropic, with 48 distinct phenotypes known compared with a median of 14 for all other genes in yeast (18). Systematic screens of gene function have described phenotypes, which are related to ribosomal dysfunction, such as a decreased growth rate in yeast extract–peptone–dextrose or in synthetic media containing glucose (19–23) as well as a reduced cell volume (24). However, there are many unrelated phenotypes reported for Δ*hpm1*, for example, an improved growth rate in alternative carbon sources (ethanol (19), xylose (25), glycerol (19), sucrose/fructose (19)), decreased desiccation resistance (26), altered vacuolar morphology (27), and altered cell wall processes (increased caspofungin resistance (28), synthetic lethality with *CHS1* (29, 30)). It is clear therefore that the function of Hpm1p, and the associated significance of Rpl3p H243 methylation, is not completely understood.

In this study, we investigate the function/s of yeast Hpm1p with a focus on its extraribosomal phenome. First, we screened Δ*hpm1* cells for growth defects on an expanded set of stressors, which targeted pathways unrelated to the ribosome. This identified undescribed sensitivities to amphotericin-B, to cold, to salt, and oxidative stress. To investigate the basis of these phenotypes, we next compared the proteome of WT and Δ*hpm1* yeast through quantitative stable isotope labeling of amino acids in cell culture (SILAC)–based proteomics. This revealed a downregulation of trehalose biosynthetic enzymes and proteins involved in glucose metabolism. Finally, we adapted the emerging technique of quantitative large-scale crosslinking mass spectrometry (MS) (31) to enable *in vivo* monitoring of the yeast interactome and structural proteome at low resolution. This revealed that *hpm1* knockout, and hence loss of Rpl3 H243 methylation, locally and allosterically alters the structure of the ribosome. Deletion of *hpm1* also affected the structure of some membrane proteins, proteins involved in chromatin compaction, and affected some protein–protein interactions (PPIs) involved in mitochondrial membrane remodeling. Importantly, these were independent of protein abundance. Orthogonal techniques confirmed alterations to processes seen in crosslinking analysis, including measurable differences to the extracellular acidification rate and mitochondrial activity. Together, these findings help explain the pleiotropy of Δ*hpm1*, expand roles for Hpm1p in the regulation of carbon metabolic processes, and

provide clues into the functional significance of histidine methylation in human and other eukaryotes.

EXPERIMENTAL PROCEDURES

Yeast Strains

WT *S. cerevisiae* were strain BY4742 (MATα [yeast maturation factor alpha] *his3*Δ1 *leu2*Δ0 *lys2*Δ0 *ura3*Δ0). The BY4742 knockout strain of *hpm1* (ordered locus name YIL110W) was derived from the EuroScarf Yeast Knockout Collection (32), with the following genotype: MATα; *his3*Δ1; *leu2*Δ0; *lys2*Δ0; *ura3*Δ0; YIL110WΔ::kanMX4. All gene and protein names throughout figures and text utilize the standard yeast protein nomenclature system, which refer to standard gene names for the encoded protein. For investigation of growth plate assay phenotype specificity, two strains were generated using homologous recombination–based genome editing in yeast (33): a pseudotype "WT*" (BY4742 containing the *URA3* gene integrated downstream of the *Rpl3* locus) and a *Rpl3* H243A mutant (also containing the *URA3* gene insertion). A custom synthetic gBlock DNA fragment (Integrated DNA Technologies) containing (1) the 3′ coding region of Rpl3, (2) immediately adjacent 3′ intergenic region, and (3) the *URA3* selection cassette, was amplified by PCR, using two primer pairs. These were the reverse primer 5′-TATTTAAATAAAATAGGAAT AAGAATGCTCAATTAAAAAATGATTTATTTTCTAACAAAACTTCTTAG TTTTGCTGGCCGCA-3′ coupled with either 5′-GCTTCCGTCGTCAG AGTTTT-3′ for *Rpl3*-H243A (to amplify the entire gBlock, including H243A mutation) or 5′-AGGTTGCTTGTATTGGTGCT-3′ for WT* (to generate a smaller amplicon, which excluded the H243A mutation). The BY4742 WT yeast strain was then transformed with each amplicon, essentially as described (34), and gene insertions and edits confirmed by PCR and Sanger sequencing using EuroScarf primers specific to the *Rpl3* locus (32).

Methyl-Peptide Analysis

Overnight cultures of saturated stationary-phase (absorbance at 600 nm of ~10) WT and Δ*hpm1* cells were pelleted, washed twice with MilliQ water, and then resuspended to 50 absorbance at 600 nm units/ml in Hepes lysis buffer (50 mm Hepes, 100 mm NaCl, 0.5% (v/v) Triton X-100, 2 mm DTT, 2 mm EDTA, pH 7.5) supplemented with Roche cOmplete Mini EDTA-free Protease Inhibitor Cocktail. Cells were lysed with three rounds of 30 s glass bead homogenization. The lysates were clarified by centrifugation at 20,000*g* for 30 min, and the supernatant resolved on a 4 to 12% Bis–Tris NuPAGE SDS-PAGE gel. In-gel digestion of a band containing the 44 kDa Rpl3p was performed with Promega Sequencing Grade Trypsin or Promega rLys-C, as described (35) but with the addition of reduction and alkylation steps (10 mM DTT at 37 °C for 1 h, followed by 55 mM iodoacetamide [IAA] at room temperature [RT] for 1 h). For LC–MS/MS analysis, online separation of peptides was performed using buffer A (0.1% (v/v) formic acid) and buffer B (0.1% (v/v) formic acid and 80% (v/v) acetonitrile), with a linear gradient of 2 to 45% buffer B over 30 min. For data-dependent analysis of the tryptic peptides, the Orbitrap Fusion Lumos Tribrid Mass Spectrometer (Thermo Fisher Scientific) was operated as described (36), with higher-energy collision dissociation;(HCD) fragmentation performed at normalized collision energy (NCE) of 30. Mascot was used to identify peptides, searching against the SwissProt reference yeast proteome (6049 sequences, accessed on December 3, 2020) for up to two missed cleavages (specificity to KR), carbamidomethylation of cysteine as a fixed modification, methylation of histidine and oxidation of methionine as variable modifications, error tolerance set to 20 ppm at the peptide level and 10 ppm at the fragment ion level, peptide charges of 2+/3+/

4+ and ESI_HCD as the instrument. Only significant peptide identifications were considered (false discovery rate [FDR] <0.01), filtering by ion score ($\geq$30) and expectation value ($p < 0.05$).

Parallel Reaction Monitoring of Histidine-Methylated Peptides

To assess the H243 modification status of Rpl3p in the WT and $\Delta hpm1$ strains, we performed a parallel reaction monitoring analysis of Lys-C peptides. The mass spectrometer was set to fragment charge states 1 to 4 of the unmodified (m/z = 867.5271, 434.2672, 289.8472, and 217.6372) and histidine-methylated (m/z = 881.5428, 441.2750, 294.5191, and 221.1412) peptide with the sequence THRGLRK. Skyline (37) (version 3.6.010493) was used to confirm the coelution of precursor and fragment ions. This analysis complies with tier 3 Molecular and Cellular Proteomics guidelines for targeted MS analysis.

Reanalysis of Heavy Methyl SILAC Datasets for Methylated Histidine

The entire heavy methyl SILAC labeling dataset (38) was reanalyzed as described in the original study but extended to include histidine methylation as an additional variable modification. Because of the high FDR associated with methyl peptides, putative histidine-methylated peptides were examined for the presence and chromatographic coelution of light/heavy methyl pairs introduced by the $^{13}CD_3$-methionine metabolic label using MethylQuant (39) and/or for the presence of the histidine methylation immonium ion (124.088 m/z) in the fragmentation spectra.

Growth Plate Assays

Synthetic complete (SC) agar medium [6.7 g/l yeast nitrogen base with ammonium sulphate, 1.92 g/l synthetic drop-out mix without uracil, 2% (w/v) glucose, 80 mg/l uracil, 3% (w/v) agar] was used for growth assays. Agar plates were prepared with or without the following chemical stressors: 2 mM H_2O_2, 0.1 µg/ml amphotericin B, 1 M NaCl, 1.5 M sorbitol, and 2 mM $NaNO_2$. Low nitrogen SC plates were prepared with 1.7 g/l yeast nitrogen base without ammonium sulphate, 1.92 g/l synthetic drop-out mix without uracil, 50 µM ammonium sulphate, 2% (w/v) glucose, 80 mg/l uracil, and 3% (w/v) agar. WT and $\Delta hpm1$ BY4742 cells were cultured overnight to saturation in yeast extract–peptone–dextrose, washed twice with sterile water, and then adjusted to an absorbance of of 0.2 at 600 nm. Five 10-fold serial dilutions were performed for each strain, and 5 µl of each was spotted onto each plate. All plates were incubated at 30 °C, except for cold stressors (16 °C and 25 °C) and heat stressors (37 °C). Plates were imaged ~72 h later, except for cold stress, salt, and H_2O_2, which required additional days of incubation to allow comparison of growth rates. Three biological replicates were performed. Growth plate assays containing all four strains (WT, $\Delta hpm1$, WT*, and *Rpl3*-H243A) were also performed in three biological replicates as described previously, but only four 10-fold serial dilutions were prepared and spotted for each strain.

2nSILAC Labeling

The 2nSILAC (isotopic labeling of lysine and arginine in prototrophic yeast) method was used to metabolically label prototrophic BY4742 *S. cerevisiae* (40). Briefly, cells were cultured for at least 12 doublings in SC labeling media containing 0.17% (w/v) yeast nitrogen base without amino acids and ammonium sulphate, 0.5% (w/v) ammonium sulphate, 20 mg/l each of histidine, leucine, methionine, tryptophan, adenine, and uracil, 200 mg/l proline, and 2% (w/v) glucose. For light-labeled cells, the media contained 287 µM L-arginine monohydrochloride and 342 µM L-lysine monohydrochloride. For heavy-labeled cells, the media contained equivalent molarity of ^{13}C, ^{15}N-labeled L-arginine monohydrochloride (+10 Da), and L-lysine monohydrochloride (+8 Da) (Silantes). To assess label incorporation efficiency, tryptic digests of heavy-labeled samples were subjected to tandem MS analysis as per the procedure described previously. Peptides were identified and quantified using MaxQuant (41) using search settings as described later, and the intensity of the heavy-labeled version of each peptide was compared with the equivalent-unlabeled peptide. Incorporation efficiency for each experiment was seen to be >99% in all 2nSILAC-labeled experiments.

Differential Proteome Analysis

To compare the proteome of WT and $\Delta hpm1$ BY4742 yeast, cells were cultured using 2nSILAC. Two biological replicates were generated in a label-swap design. Each strain was grown in 35 ml of heavy or light media and harvested at a midlog phase at an absorbance of ~0.8 at 600 nm. To extract proteins, cells were resuspended at 50 absorbance at 600 nm units/ml of lysis buffer (8 M urea, 0.1 M ammonium bicarbonate, and pH 8), supplemented with Roche cOmplete Mini EDTA-free Protease Inhibitor Cocktail, and subjected to glass bead homogenization for three rounds of 30 s each. The lysates were clarified by centrifugation at 20,000*g* at 4 °C for 30 min. The Pierce Bicinchoninic Acid Protein Assay Kit was used to determine the protein content in each lysate. Lysates were mixed 1:1 in a label-swap design, to 1 mg total protein content (500 µg each). Reduction was performed using 5 mM DTT for 30 min at RT, followed by alkylation with 10 mM IAA for 30 min at RT in the dark. To facilitate digestion, each sample was diluted 10-fold with 50 mM ammonium bicarbonate and digested overnight at 37 °C with Promega Sequencing Grade Trypsin at a 1:100 protease:protein ratio. Peptides were desalted using C18 Sep-Pak columns, as described (31), and then subjected to strong cation exchange (SCX) fractionation as described later in SCX to yield five fractions per combined light/heavy sample for analysis. Fractions resulting from SCX chromatography were desalted using Sep-Pak columns, again as described (31). Desalted fractions were resuspended in 20 µl 0.1% (v/v) formic acid and injected in technical duplicate for LC–MS/MS analysis. Online fractionation was performed as described for methyl-peptide identification, albeit with a 120 min gradient. The Fusion Lumos mass spectrometer was operated with the following settings: MS1 spectra were acquired at 120,000 resolution, scan range 400 to 1500 m/z, RF lens 30%, and 50 ms maximum injection time. The most abundant ions were selected for fragmentation using monoisotopic precursor selection mode, 2.5E4 intensity threshold, z = 2 to 5, 20 s dynamic exclusion, across a 3 s duty cycle. Ions were fragmented using HCD fixed at 30% NCE with a 1.6 m/z isolation window, acquiring spectra with the ion trap mass analyzer in rapid mode.

MaxQuant (41) (version 1.6.17.0) was used to both identify and quantify peptides, matching against the SwissProt reference yeast proteome (6049 sequences, downloaded December 3, 2020) supplemented with the default contaminants database. Relevant settings included use of the heavy label feature set to Arg10 and Lys8, variable modification of methionine oxidation and acetylation of the protein N terminus, fixed modification of cysteine carbamidomethylation, the use of trypsin/P specificity with a maximum of two missed cleavages, a minimum peptide length of 7, FDR limited to 1% at both the peptide and protein levels, and only unique + razor peptides (at least two) used for quantification. All other settings were default. An additional analysis for lysine acetylation was performed as previously mentioned one but with the addition of lysine acetylation as a variable modification. For differential abundance analysis, the resulting evidence.txt and proteingroups.txt files were analyzed using the aggregation, normalization, and differential expression analysis tools in ProteoSign, v2 (42). Default parameters were used, which only consider proteins quantified

in both biological replicates and with at least two different peptides. Significance of expression ratios was assessed between biological replicates (at adjusted $p \leq 0.05$), after determining ratios from technical replicates and between-fraction replicate identifications.

SCX of Peptides and Cross-Linked Peptides

Desalted peptides were fractionated using the Agilent 1260 Infinity II HPLC, coupled to a Phenomenex Luna 5um SCX 100Å 250 × 10 mm LC column, and using buffer A containing 7 mM KH_2PO_4, pH 2.6, and 30% (v/v) acetonitrile, and buffer B containing 7 mM KH_2PO_4, pH 2.6, 30% (v/v) acetonitrile, and 350 mM KCl. The gradient was as operated at 1.5 ml/min with the following program: 0% B at 0 min, 5% B at 7.5 min, 60% B at 47.5 min, 100% B at 67.5 min, 100% B at 77.5 min, 0% B at 77.51 min, and 0% B at 97.5 min. For the proteomics experiments, individual 1-min fractions were combined into five final pooled fractions from the following elution times: F1 = 10 to 39 min, F2 = 39 to 48 min, F3 = 48 to 58 min, F4 = 58 to 72 min, and F5 = 72 to 89 min. For the crosslinking experiments that are described in later sections, later eluting peptide fractions enriched for cross-linked peptides were combined into five final fractions as follows: F6–F7 = 48 to 53 min, F8–F9 = 58 to 63 min, F10 = 68 to 73 min, F11 = 73 to 78 min, F12 = 78 to 83 min, and F13 to F15 = 83 to 93 min.

Functional Enrichment Analysis

Panther Gene Ontology (GO) Term Over Representation analysis (43) was performed on the results of the differential proteome analysis, using an expanded list of proteins (adjusted $p \leq 0.1$) The background was set to all quantified proteins. Biological Process Complete GO terms were analyzed, with the Fisher's exact test and FDR calculated and controlled to 5%. Only the significant child terms were reported to avoid redundancy.

Biotin–Aspartate Proline–N-Hydroxyphthalimide Cross-Linker Synthesis

The peptide-based cross-linker biotin–aspartate proline–*N*-hydroxyphthalimide (BDP–NHP) was synthesized using Fmoc chemistry as described (31) but with the use of Rink amide ProTide resin (CEM) instead of Fmoc-Gly-Wang resin. Amino acids were coupled to the resin in the following order: Lys(biotin)-Lys-Pro$_2$-Asp$_2$-succinate$_2$-*N*-hydroxyphthalimide (NHP)$_2$, using a Liberty Lite peptide synthesizer (CEM). Activated NHP esters were incorporated by incubating the resin containing the BDP molecule with a 12-fold molar excess of *N*-(trifluoroacetoxy)-phthalimide–NHP in pyridine. The reaction was carried out for 20 min at RT. The resin was then transferred to a PolyPrep column (Bio-Rad) and coupled to a vacuum flask. The resin was washed extensively with dimethylformamide followed by extensive washes with dichloromethane. The crosslinker was cleaved from the resin by incubation with 95% *N*-(trifluoroacetoxy), 2.5% dichloromethane, and 2.5% H_2O for 3 h at RT. The crosslinker was then precipitated in cold diethyl ether and washed extensively with fresh cold diethyl ether. The resulting pellet was dried by vacuum centrifugation. The resulting product was dissolved in dimethyl sulfoxide to a concentration of 200 mM, determined by UV–visible absorbance.

In Vivo CrossLinking MS

WT and Δ*hpm1* cells were cultured using the 2nSILAC approach, with each strain grown in 200 ml of light- or heavy-labeled media. Cells were harvested at a midlog absorbance of ~0.4 at 600 nm and washed with water. An aliquot of each was taken to confirm label incorporation efficiency, which was found to be >99%. Cells were then mixed 1:1, based on an absorbance at 600 nm, in a label-swap design, and then

followed by an additional wash with water. To enzymatically digest the cell wall, cells were first pretreated with 10 mM DTT and 100 mM Tris for 10 min at 30 °C with shaking. After washing with water, cells were resuspended in 2 ml 1.2 M sorbitol supplemented with 300 U/ml zymolyase and incubated for 30 min at 30 °C with light shaking. The progression of cell wall digestion (spheroplasting) was monitored *via* microscopy and through monitoring of lysis with a 1:20 dilution in water. Spheroplasts were pelleted at 750*g*, washed with 1.2 M sorbitol twice, and then resuspended in crosslinking buffer (1.2 M sorbitol, 170 mM Na_2HPO_4, pH 8). Protein interaction reporter (PIR) (amide-BDP–NHP) crosslinker was added to 10 mM, and the reaction allowed to proceed for 30 min at RT with shaking. Cross-linked spheroplasts were washed five times with 1.2 M sorbitol until the supernatant was no longer yellow and then resuspended in lysis buffer (8 M urea, 0.1 M ammonium bicarbonate, and pH 8.0). This was followed by lysis *via* glass bead homogenization for three rounds of 30 s each. A bicinchoninic acid assay was used to quantify protein content, and then 3 mg of each lysate was reduced with 5 mM DTT for 30 min at RT, followed by alkylation with 10 mM IAA for 30 min at RT in the dark. The sample was diluted 1:10 with 0.1 M ammonium bicarbonate and digested with Promega Sequencing Grade Trypsin at a protease:protein ratio of 1:50, overnight at 37 °C with shaking 650 rpm. Peptides were desalted using a Sep-Pak column, and a 100 μg aliquot taken for protein abundance level quantification, using the same MS scheme described earlier for the proteomics analysis. The remaining peptides were fractionated by SCX as described previously, generating five final fractions per light/heavy sample. Cross-linked peptides from each fraction were enriched with Pierce Monomeric Avidin UltraLink beads, as described (31), *via* the biotin group in the BDP–NHP crosslinker.

Each of the five avidin-enriched fractions was injected twice and analyzed on the 120 min liquid chromatography gradient described previously. The Fusion Lumos mass spectrometer was operated with the following settings: MS1 spectra were acquired in positive ion mode, 60,000 resolution with quadrupole isolation, scan range 400 to 2000 *m/z*, RF lens 30%, 100 ms maximum injection time, automatic gain control target set to "Standard." Ions were selected for fragmentation using monoisotopic precursor selection mode, 2.5E4 intensity threshold, z = 4 to 8, 20 s dynamic exclusion, across a 2 s duty cycle. Ions were fragmented using stepped HCD (27/30/33 NCE) with a 1.6 *m/z* isolation window, acquiring spectra with the Orbitrap analyzer at 60,000 resolution.

The Mango/Comet/XLinkProphet pipeline was used to identify cross-linked peptides. RAW files were first converted to mzXML (with peak picking at both MS levels) using MSConvert (ProteoWizard, version 3.0.1908) (44). Spectra that contained putatively cross-linked peptides were extracted using the Mango tool (version 2017.01 rev 0 beta 3) (45), with the reporter neutral mass set to 693.399601 Da and the mass tolerance at the relationship level set to 10 ppm and peptide level set to 20 ppm. Fragment ions in these spectra were matched against the yeast reference proteome (6049 sequences, downloaded December 3, 2020), alongside a reverse decoy database, using the search engine Comet (version 2018.01 rev 2) (46), performing two individual searches for each file to identify completely light or heavy isotopically labeled peptides. Key Comet parameters were set as follows: 20 ppm parent and fragment ion tolerance, cysteine carbamidomethylation as a fixed, methionine oxidation as variable, and the cross-linker stump mass of 197.032422 Da on lysines as variable, up to two missed tryptic (KR, negated by P) cleavages allowed. XLinkProphet (47) was used with default recommended parameters to recombine spectral matches and perform FDR control of identifications to a 1% error rate at the nonredundant cross-linked peptide level. These identifications were uploaded to the XLinkDB (48) under the name "YeastHpm1_Wilkins." For mapping of crosslinks onto

structure, all possible structures involving the cross-linked residues were downloaded from the Protein Data Bank (PDB) (rscb.org (49)) and crosslinks mapped in every chain pair configuration using Xwalk (50), to calculate the minimum Cα–Cα Euclidean distances imposed by the given crosslinks. The SIFTS resource was used to determine PDB resolved residues (51). A random lysine–lysine pair list was generated by randomly selecting any lysine residue in each protein member of an experimentally identified crosslink that mapped to that structure. The Euclidean distances of these links were also evaluated.

Cross-link spectral matches (CSMs) from these identified cross-linked peptides were subjected to analysis with MethylQuant (39) tool (version 1.0) to automatically extract ion chromatograms. The derived light and heavy *m/z* values were used as input, using default program parameters, but without the use of the in-built mass shift function. The MethylQuant output was filtered for only crosslinks with successful "H/L Ratio #2" ratios (which are MethylQuant ratios that passed an internal quality control based on the presence of highly correlated isotope coelutions) and a MethylQuant score greater than 10. Crosslinks involving methionine were not analyzed further. The cross-link ratios within each biological replicate were normalized (to correct for unequal mixing in sample preparation) by dividing each ratio, before log transformation, by a protein mixing factor. The mixing ratio factor was determined from a matched proteomic analysis of the samples before fractionation, with each sample acquired in the same manner as the deep proteome MS/MS described previously except in one shot. Note that this proteomic dataset was also used to determine changes in protein abundances, for comparing crosslink changes with changes in protein abundance.

To summarize changes in crosslinks to the level of unique residue pair (URP), redundant normalized ratios from cross-linked peptides were averaged to form a single ratio per biological replicate (where redundant ratios could represent multiple peptide pairs representing the same URP, quantification in different fractions, or technical replicates). Only URPs with ratios successfully calculated from both biological replicates were considered further, whereby the average of biological replicates was used for statistical testing. To determine statistical significance, two-tailed unpaired *t* tests were performed by comparing ratios to 0. Multiple testing correction was performed using Boca and Leek's FDR regression method (BL) as implemented in the *swfdr* R package (52). Briefly, a linear regression with spline smoothing (two degrees of freedom) was modeled on *t* test *p* values and three covariates to generate *q* values. The three covariates were correlated to the quality of the quantifications themselves: (1) the standard deviation of all technical replicate redundant ratios for the URP, (2) the total number of redundant ratios calculated for the URP, and (3) the maximum number of well-correlated isotopic distribution heavy/light pair coelutions (as determined by MethylQuant) for any quantification representing the URP. To compare URP ratios with protein-level change, the URP ratios for significantly changing URPs ($q \leq 0.05$, $\log_2 \geq 0.3$ and ≤ -0.3) were compared with the mean normalized protein ratio for the given protein/s, determining statistical significance using the two-tailed unpaired *t* test and then BL multiple testing correction as described previously. Cytoscape (53) was used to visualize crosslinks as either a protein interaction network or a residue-pair network. PyXlinkViewer (54) was used to map crosslinks onto the ribosome structure (PDB: 6GQV (55)).

Monitoring of Media Acidification Rate

To monitor changes to media pH over time, three independent colonies each of WT and Δ*hpm1* were separately cultured overnight to saturation in SC medium (6.7 g/l yeast nitrogen base without amino acids, 1.92 g/l synthetic drop-out mix without uracil, 2% [w/v] glucose, and 80 mg/l uracil). For each sample, 50 ml cultures of SC media were inoculated at an initial absorbance at 600 nm of ~0.1 and cultured at 30 °C with 250 rpm shaking for 11 h. An aliquot was taken every hour to determine an absorbance at 600 nm and, following pelleting of cells, the pH of media was measured by a tabletop pH probe. For each strain, a one-phase nonlinear regression curve was fitted to data from the three biological replicates using GraphPad Prism 9.3.1 (GraphPad Software, Inc). To determine whether the two models differed (whether one model could adequately explain all data), the extra-sum-of-squares *F* test was used, comparing all equation parameters.

Flow Cytometric Analysis of Mitochondrial Activity

To determine the degree of mitochondrial superoxide production in the WT and *hpm1* knockout strains, yeast cells were stained with MitoSOX Red Mitochondrial Superoxide Indicator dye (Thermo Fisher Scientific) and assessed by flow cytometry. Briefly, three independent colonies of each strain were grown separately to saturation overnight in SC medium, cultured throughout the day to produce a growth curve, and inoculated into 25 ml of fresh SC for overnight culture. Cells were harvested the following morning at an absorbance of ~0.7 at 600 nm, washed twice with PBS, and then resuspended to a density of 10 absorbance at 600 nm units/ml in PBS. Unstained and stained (5 μM MitoSOX 10 min at RT in the dark) cells were prepared for each strain, with two additional PBS washes performed before analysis on the BD LSRFortessa SORP Cell Analyzer (BD Biosciences). Following gating to select for single cells, the mean intensity of the staining (10,000 cells per sample) was measured using the 561 nm Yellow/Green laser with 610/20 band pass filter. The mean population intensity of unstained samples was subtracted from the mean population intensity of the matched labeled samples, and a two-tailed unpaired *t* test was used to assess statistical significance.

Experimental Design and Statistical Rationale

Four independent cultures (two of each of the control WT and Δ*hpm1* strains in heavy or light media) were used in SILAC expression or crosslinking experiments, producing two biological replicates in a label-swap design (forward: light = WT, heavy = Δ*hpm1*; reverse: light = Δ*hpm1*, heavy = WT). Five SCX fractions were generated per light/heavy combined biological replicate, and each SCX fraction was analyzed in technical duplicate, being injected twice for LC–MS/MS analysis. Data processing and statistical analyses for each investigation type are described in detail previously.

RESULTS

Confirmation of the Rpl3p H243 Methyl Site and Determination of Stoichiometry

Amino acid analysis and mutational analysis had previously shown that methyltransferase Hpm1p catalyzes the methylation of H243 (H243$_{Me}$) on the large ribosomal subunit protein L3 (Rpl3p) (Fig. 1*A*). However, efforts to detect this modification by MS had only localized it to an 18-residue window of G234 to C251 (11). To confirm Hpm1p-mediated H243$_{Me}$, in-gel tryptic digestion of Rpl3p from whole-cell lysates was performed, and the resultant peptides were analyzed by LC–MS/MS. This identified the methylated peptide KTH$_{Me}$RGLR and precisely localized the methylation to residue 243 (supplemental Fig. S1). Notably, the identified spectrum contained a 124.088 *m/z* immonium ion (supplemental Fig. S1, *inset*), which has recently been described as diagnostic for histidine methylation (10). To generate a peptide with no missed cleavages and thus more suitable for quantification, we
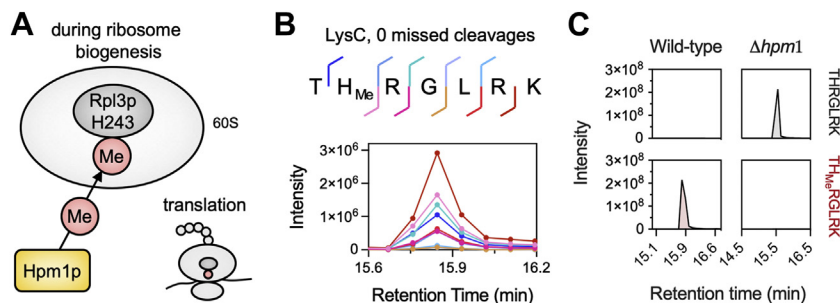
FIG. 1. **Identification of Rpl3p H243$_{Me}$ by bottom–up mass spectrometry.** *A*, the histidine methyltransferase Hpm1p monomethylates histidine 243 of the large ribosomal subunit protein Rpl3p. The methylation site of Rpl3p directly contacts the 25S rRNA and is in proximity to the ribosomal peptidyl transferase center. *B*, PRM analysis of the LysC generated, Rpl3p methylated peptide TH$_{Me}$RGLRK (2+, 443.2672 *m/z*), showing codetection of the fragments at the same retention time. *C*, extracted ion chromatograms of the precursors for the THRGLRK (2+, 441.2750 *m/z*) and TH$_{Me}$RGLRK (2+, 443.2672 *m/z*) peptides, generated from LysC digest of the Rpl3p band in WT or Δ*hpm1* lysate. H243$_{Me}$, methylation of histidine 243; Hpm1p, histidine protein methyltransferase 1; PRM, parallel reaction monitoring.

digested proteins with Lys-C. Targeted MS/MS analysis of the peptide TH$_{Me}$RGLRK showed chromatographic coelution of the parent and fragment ions and further confirmed that the methylation site is localized to H243 (Fig. 1*B*). Analysis of the unmethylated and methylated forms of the LysC-generated peptide from WT cells confirmed that this modification reaches stoichiometric (>99.9%) levels on Rpl3p *in vivo* (Fig. 1*C*). By contrast, methylation on this peptide in *hpm1* knockout cells is completely absent, proving that Hpm1p is the sole methyltransferase responsible for this modification.

There have been conflicting reports (15, 16) on whether Rpl3p is the only substrate of Hpm1p. We therefore investigated whether additional histidine methylation sites could be detected, by reanalyzing a published heavy-methyl-SILAC, yeast deep proteome dataset (38). Heavy-methyl-SILAC enables high confidence discovery of methylated residues by analyzing a mixture of unlabeled and $^{13}CD_3$-methionine-labeled peptides (56). FDRs, a known issue in the discovery of methylation sites (38), can be reduced through correlative analysis of isotopic peaks in SILAC pairs and their chromatographic coelution profiles (39). Our analysis did not detect any histidine-methylated peptides (data not shown). This included the TH$_{Me}$RGLRK Rpl3p peptide; however, this is produced from two missed tryptic cleavages and therefore difficult to detect within complex lysates. Further analysis of all data for the 124.088 *m/z* diagnostic immonium ion also did not detect any histidine-methylated peptides. Therefore, at least in a comprehensive tryptic peptide set, we were not able to find any evidence that Hpm1p catalyzes methylation of histidine residues anywhere in the yeast proteome, except on Rpl3p as described above and in Ref. (11).

Deletion of the hpm1 *Gene Results in Sensitivity to Environmental Stressors*

The deletion of *hpm1*, and hence loss of Rpl3p H243 methylation, is known to result in ribosome-related defects (11, 15–17). To further characterize the phenotype of this knockout, we subjected WT and Δ*hpm1* yeast to a range of environmental stressors (Fig. 2). This revealed growth defects of Δ*hpm1* under oxidative stress (2 mM H_2O_2), membrane stress (0.1 μg/ml amphotericin B), salt stress (1 M NaCl), and cold stress (16 °C, RT). All other stressors tested, including heat stress (37 °C), low nitrogen media, osmotic stress (1.5 M sorbitol), and nitrosative stress (2 mM $NaNO_2$), did not increase or decrease the growth rate of the *hpm1* deletion mutant. To further investigate whether H243 methylation on Rpl3p specifically mediated these responses, we constructed the Rpl3p-H243A point mutant and compared its growth with a matched WT control that also contained the *URA3* selection cassette used in our genome editing (supplemental Fig. S2). Interestingly, this revealed that the H243A mutant phenocopied the *hpm1* knockout sensitivity for some stressors (cold and salt stress) but that only the *hpm1* knockout was sensitive to other stressors (H_2O_2 and amphotericin). This observation has parallels with those of the study by Al-Hadid *et al.* (16), who saw perturbed levels of ribosomal subunits in *hpm1* knockout cells but not in Rpl3p-H243A. Our results show that loss of Hpm1p is associated with sensitivity to a number of environmental stressors and clear extraribosomal phenotypes.

Protein Abundance Profiling Identifies a Role for Hpm1p in Carbon Metabolism

To investigate the reasons for the aforementioned Δ*hpm1* growth phenotypes, and others previously reported, we compared the proteome of WT and Δ*hpm1* yeast (Fig. 3*A*). To do so, we cultured each strain in media containing either unlabeled lysine and arginine (light) or heavy-isotope labeled lysine and arginine (heavy, +8 and +10 Da, respectively). We confirmed efficient (>99%) incorporation of heavy lysine and heavy arginine in isotopically labeled cultures (supplemental Fig. S3) and controlled for mixing by normalizing ratios. In a double label-swap SILAC design, MaxQuant (41) identified 55,113 unique peptides (length ≥7 amino acids) at 1% FDR
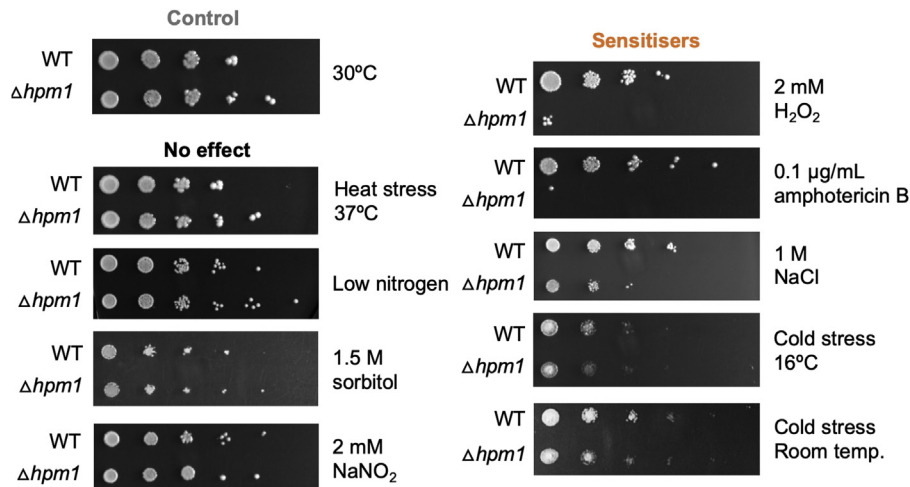
FIG. 2. ***hpm1* knockout sensitizes yeast to cold, to oxidative, and cell membrane stress.** WT and *hpm1* knockout BY4742 *Saccharomyces cerevisiae* were cultivated in liquid cultures overnight to saturation, adjusted to 0.2 absorbance at 600 nm, and serially diluted 1:10 five times. Five microliters of each dilution was spotted onto synthetic complete agar plates with cold, heat, oxidative, salt, osmotic, or cell membrane stressors. Hpm1p, histidine protein methyltransferase 1.

from five SCX fractions per biological replicate, analyzed in technical duplicate. This corresponds to 3801 unique protein groups with at least two unique peptides (supplemental Table S1). The knockout status of the Δ*hpm1* BY4742 was confirmed, with ion intensity from peptides in Hpm1p (LVTIPNLVITWAK, LTFEEFQSPIYR, EQWYALQKDECEDI-PINNEELLLTSK) only identifiable and quantifiable in the WT strain (data not shown). Proteins with at least two successfully quantified peptides were subjected to statistical analysis, which revealed 11 proteins changing with significance (adjusted p value ≤ 0.05), all of which had $\log_2$ fold change $>\pm 1$ (supplemental Table S2). One protein was upregulated, Tdp1p. The downregulated proteins included glycolysis enzymes Emi2p, Hxk1p, and Glk10p, trehalose synthesizing enzymes Tps2p and Tsl1p, glucose-regulated protein Ygp1p, and proteins in other systems, such as Rep2p, Pho84p, Sse2p, and Rtc3p (Fig. 3*B*). Functional enrichment analysis on a more extensive list of 24 proteins with adjusted p values ≤ 0.1 identified several processes broadly related to carbon metabolism with statistical significance (Fig. 3*C*). These were cellular response to desiccation (GO: 0071465), trehalose biosynthetic process (GO: 0005992), cellular glucose homeostasis (GO: 0001678), carbohydrate phosphorylation (GO: 0046835), glucose 6-phosphate metabolic process (GO: 0051156), and carbohydrate catabolic process (GO: 0016052). Furthermore, mapping of proteome changes to all members of the trehalose synthetic pathway (Tsl1p, Tps1p, Tps2p, and Tps3p) revealed general downregulation of this metabolic pathway in Δ*hpm1* (Fig. 3*D*). Our results relate to previous observations from large-scale screens that Δ*hpm1* yeast grow faster than WT cells on media containing nonfermentable carbon sources, such as xylose (25), glycerol, and ethanol (19). These carbon sources allow cells to either entirely avoid glycolysis or be more reliant on metabolic pathways such as

oxidative phosphorylation. All four known members of the trehalose synthetic pathway (Tsl1p, Tps1p, Tps2p, and Tps3p) were downregulated in Δ*hpm1* (Fig. 3*D*).

Differential In Vivo *Crosslinking of* S. cerevisiae *Proteins*

hpm1 deletion cells are hypersensitive to membrane, oxidative, and salt stress (Fig. 2). These phenotypes were not readily explained by changes in protein abundance but may arise because of changes in PPIs or gross changes in protein structures. To investigate this, we adapted the PIR *in vivo* crosslinking approach (31) for use in *S. cerevisiae*, which employs the lysine-reactive and MS-cleavable crosslinker BDP–NHP (Fig. 4*A*). This was achieved through (1) use of 2n native SILAC metabolic labeling and (2) addition of an enzymatic digestion step of whole yeast with zymolyase to permeabilize the cell wall to the PIR crosslinker. Our experiment represents the first *in vivo* large-scale crosslinking MS analysis of budding yeast, and one which uses an enrichable and MS-cleavable crosslinker.

To compare WT and Δ*hpm1* cells using this approach, cells were metabolically labeled and then mixed in a label-swap design before downstream spheroplasting, crosslinking, and protein extraction. Tryptic digests of lysates were fractionated using SCX and crosslinker-reacted peptides then enriched with monomeric avidin beads, generating five fractions per biological replicate. These were analyzed with LC–MS/MS by stepped HCD in technical duplicate. The Mango/Comet/XLinkProphet pipeline confidently identified 1889 nonredundant cross-linked peptide pairs at a 1% FDR (controlled at the nonredundant cross-linked peptide level) (supplemental Table S3). This represented 1267 URPs, of which 261 (21%) were interprotein links and 1006 (79%) were intraprotein links. Redundancy observed in raw CSMs was due to SILAC labeling (doubled by the presence of heavy-labeled CSMs) and
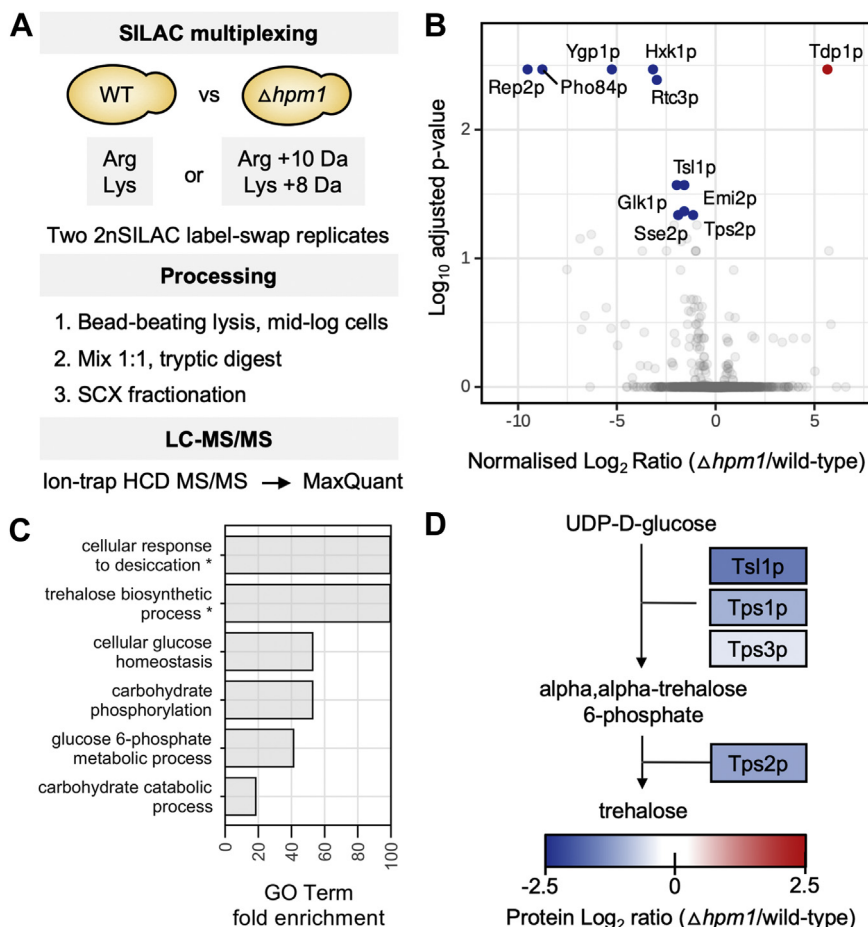
Fig. 3. **Proteomic analysis identifies changes to sugar metabolism upon *hpm1* knockout.** *A*, label-swap replicates prepared by 2nSILAC (arginine +10, lysine +8) were used to compare the steady-state proteome of log-phase WT and Δ*hpm1*. The tryptic digests were fractionated by SCX and then subjected to high-resolution HCD MS/MS analysis on a Fusion Lumos. *B*, results of the differential proteome abundance analysis. Labeled proteins have an adjusted *p* value ≤0.05 and log$_2$ fold change ≥1 or ≤−1. *C*, statistically significant child terms resulting from a Panther Biological Process GO term overrepresentation analysis using 24 proteins as input (adjusted *p*≤ 0.1), with all quantified proteins used as background. Changing GO terms are annotated, and the asterisk * represents enrichment fold changes >100. *D*, proteins involved in the trehalose biosynthetic pathway, with protein log$_2$ changes overlaid by color. 2nSILAC, isotopic labeling of lysine and arginine in prototrophic yeast; GO, Gene Ontology; HCD, higher-energy collision dissociation; SCX, strong cation exchange.

a high degree of URP overlap (46%) between biological replicates (Fig. 4*B*).

We first explored the identified URPs in terms of structural information and PPIs. The intralink URPs represented 1006 *in vivo* structural constraints for 251 unique proteins. Mapping of all (interprotein and intraprotein) URPs onto an ensemble of PDB structures showed that 93% of the 543 mappable URPs fell within the 42 Å theoretical distance constraint of the PIR crosslinker (Fig. 4*C*). Notably, the distribution of Euclidean distances imposed by random lysine–lysine links in these PDB structures was much broader, with only 49% falling within the PIR distance cutoff. Unmappable intraprotein URPs represent valuable information for proteins, which have no experimental structure or where part of the available structure is unresolved. An additional 261 URPs represented 146 unique *in vivo* PPIs, including homodimers (Fig. 4*D*). Twenty-six unique PPIs were of very high confidence (with more than one CSM) and also

novel (without curation in the APID protein interaction database (57)). An example is the interaction between the uncharacterized protein YKR015Cp and histones H3 and H2B.

To investigate the effect of *hpm1* knockout on the structural proteome and interactome, as measured by crosslinking MS, light- and heavy-labeled cross-linked peptides were quantified by generating extracted ion chromatograms in MethylQuant (39). This was possible for 877 URPs, with 390 URPs quantified in both replicates (Figs. 5*A*, S4 and supplemental Table S4). Of these 390, 60 URP ratios changed significantly (*q* value ≤0.05, log$_2$ ratios ≥0.3 and ≤−0.3), indicating the modulation of a protein's structural conformation or PPI. We investigated whether there were URPs that were unique in the WT or *hpm1* knockout strains. To do this, we asked if there were exclusively quantifiable URPs in one strain, and furthermore, if they were reproducibly unique in label-swap replicates. We were not able to detect any such crosslinks in our
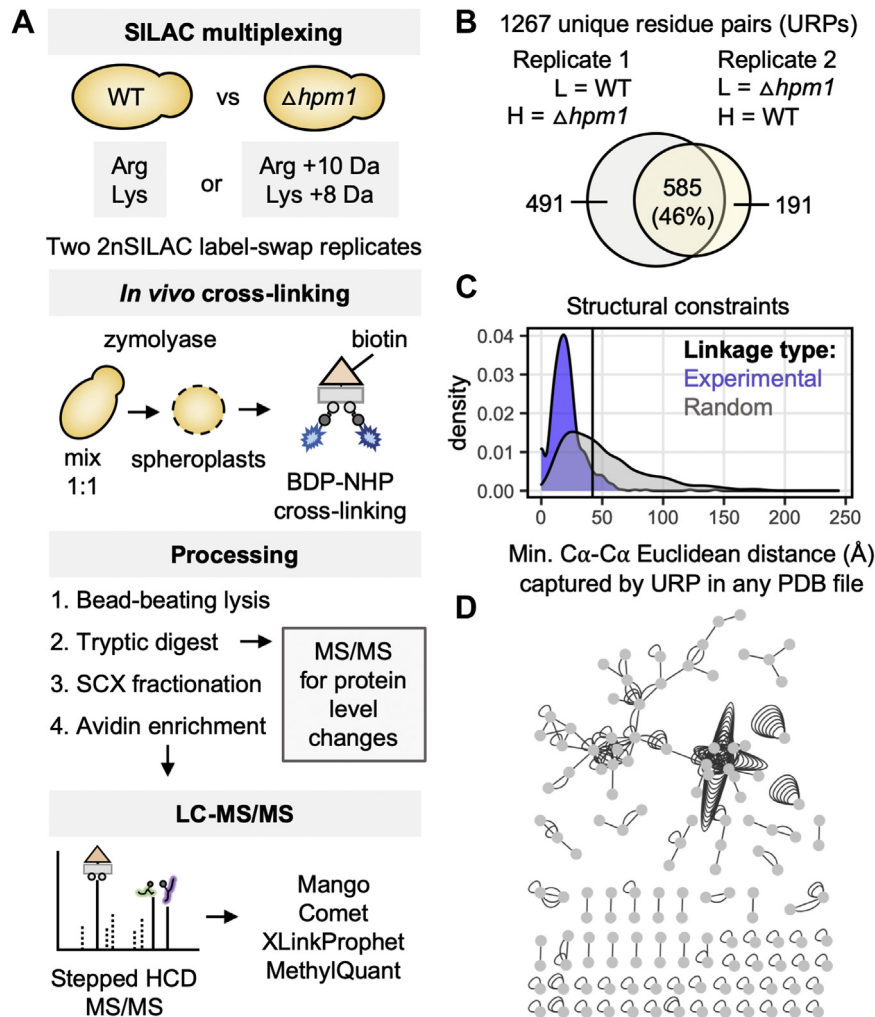
FIG. 4. Large-scale crosslinking mass spectrometry (MS) for the monitoring of *in vivo* protein structure and interactions in *Saccharomyces cerevisiae*. *A*, experimental overview of quantitative crosslinking MS to compare WT and Δ*hpm1* cells, adapted for use with *S. cerevisiae* by the enzymatic digestion of the yeast cell wall to increase permeability to the MS-cleavable crosslinker BDP–NHP (PIR). A sample was taken before SCX fractionation, for single-shot proteomic analysis and to normalize crosslinking data for changes in protein abundance. *B*, overlap of unique residue pair (URP) identifications between biological replicates. *C*, density histogram of minimum distances for 543 interprotein and intraprotein URPs, and random lysine-lysine pairs, when mapped to 794 possible cognate PDB structures. *D*, protein interaction network (including unambiguous homodimers) represented by the identified URPs. Nodes are unique proteins, and edges are URPs. BDP–NHP, biotin–aspartate proline–*N*-hydroxyphthalimide; PDB, Protein Data Bank; PIR, protein interaction reporter; SCX, strong cation exchange.

analysis. We also asked whether there was evidence of crosslinking between heavy- and light-labeled peptides, which may arise from the mixing of proteins from cells before crosslinking occurred. There were only 51 of 21,978 (0.23%) spectra with PIR ions where the individual peptides were of different label (at a PSM FDR of 1%).

To confirm that changes in cross-link abundance were not simply a result of differential protein abundance, we also analyzed the proteome of the cross-linked spheroplasts (Fig. 4A and supplemental Table S5). Note that this is a separate analysis to that which was presented previously (Fig. 3), which was performed on the non–cross-linked and nonspheroplasted proteome. This revealed that most proteins were not changing in abundance between WT and Δ*hpm1*

yeast (supplemental Fig. S5). A direct comparison of the 60 significant URP ratios to the mean protein level ratio of the cognate proteins, obtained from the parallel proteomic analysis, revealed that 44 URPs changed (q value ≤0.05) beyond the level of protein abundance changes (Fig. 5B and supplemental Tables S6 and S7).

Quantitative Changes in Crosslinks are Associated With Phenotypes of Δhpm1

We examined the cases where URPs changed in abundance beyond detected changes in abundance of cognate proteins. The ratios of changed interprotein and intraprotein URPs and of their proteins are given in supplemental Tables S6 and S7, respectively. Interestingly, some of the
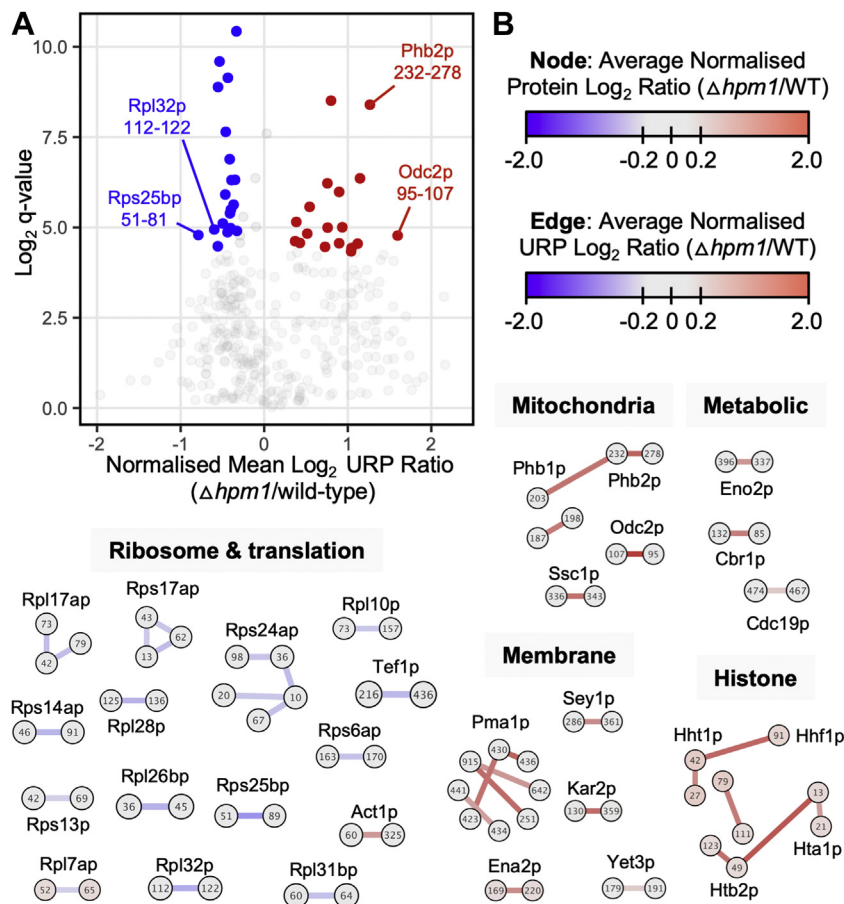
FIG. 5. **Quantitative large-scale crosslinking reveals modulation of the structural proteome and interactome in *hpm1* knockout yeast.** *A*, volcano plot showing Δ*hpm1*/WT ratios for 390 URPs, successfully quantified in both biological replicates. Crosslinks were averaged across biological replicates to form the URP log₂ ratio, after normalization for mixing as determined by the matched proteomics experiment. Statistical significance was determined using a two-tailed unpaired *t* test, with BL multiple testing correction. Colored URPs have *q* values ≤0.05 and log₂ ratios ≥0.3 or ≤−0.3. About 37 URPs with extreme *q* values been excluded from this plot to aid visualization of most URPs. *B*, lysine–lysine network view of URPs with statistically significant change, after adjustment for changes in cognate protein(s). Nodes contain lysine residue numbers, with the associated protein name annotated in proximity. Ratios of change are overlaid in color for both protein levels (on nodes) and URPs (on edges). BL, Boca and Leek's FDR regression method; URP, unique residue pair.

observed changes related to key phenotypes of the Δ*hpm1* knockout. These included a phenotype of decreased expression of many proteins in the proteome (Fig. 3*B*), and changes to proteins in membranes, the mitochondria, and some metabolic processes. For example, our crosslinking indicated that Δ*hpm1* cells may modulate some transcriptional processes (and hence the proteome) through changes to chromatin. URP interlinks involving the histone subunits increased in abundance in the knockout strain (Fig. 5*B*), suggesting chromatin compaction. Consistent with these observations, reinvestigation of our proteomic data revealed that acetylation of histone Hta1/2p lysine 8 (H2AK7ac, from the tryptic peptide SGGKGGK_AcAGSAAK), a transcriptionally activating epigenetic modification (58, 59), was downregulated in the knockout strain, with a Δ*hpm1*/WT log₂ ratio of −1.03 (data not shown). As noted, this reflects what we observed in our non–cross-linked proteome analyses where most differentially

abundant proteins, and indeed the majority of other proteins we quantified, were downregulated on *hpm1* knockout (Fig. 3*B*). By contrast, no clear changes were detected in the abundance of other acetylated histone peptides including in Htb1p-K12 (H2BK11ac, from KPASK_AcAPAEK) and Htb2p-K7 and Htb2p-K8 (H2BK6ac from SSAAEK_AcKPASK and H2BK7ac from SSAAEKK_AcPASK, respectively).

In a different phenotype, wherein Δ*hpm1* yeasts were sensitive to the membrane stressor amphotericin B (Fig. 2), we noted a relationship with changed URPs. URP intralinks identified within the plasma membrane–embedded ATPase Pma1p, and in the endoplasmic reticulum chaperone Kar2p, were greatly increased in the Δ*hpm1* strain. In addition, there were changes to intralink URPs within the Yet3p and Sey1p proteins, which also reside in the endoplasmic reticulum. In a further example, there was an intralink URP change in the plasma membrane sodium transporter Ena2p, which may

reflect the increased sensitivity of this strain to salt stress (Fig. 2). Interestingly, we were able to detect structural changes in enzymes involved in glucose metabolism, which may reflect the changes to metabolic processes detected in Figure 3. This included the cytochrome b reductase Cbr1p, the pyruvate kinase Cdc19p, and phosphopyruvate hydratase Eno2p, which are involved in gluconeogenesis and glycolysis.

Mitochondrial dysfunction is known to increase the sensitivity of yeast to reactive oxygen species, such as that in the 2 mM H_2O_2 treatment, which reduced $\Delta hpm1$ growth in our plate assays (Fig. 2). The mitochondrion is also essential for respiration, necessary for growth on alternative carbon sources. Interestingly, some URPs involved in mitochondrial membrane protein sorting (Phb1p and Phb2p) showed significant change (Fig. 5B). For the proteins prohibitin 1 and 2, the cross-linked peptide FLVEKAEQER-AAFVVDKAR represented in the Phb1p-203:Phb2p-232 URP, increased in $\Delta hpm1$ yeast ($\Delta hpm1$/WT log$_2$ ratio of 1.1). However, the Phb1p and Phb2p proteins themselves did not change in abundance, with $\Delta hpm1$/WT log$_2$ ratios of −0.08 and −0.01, respectively. Hence, the PPI between prohibitin 1 and 2, known to be involved in many mitochondrial membrane functions including protein chaperoning (60), increased in $\Delta hpm1$ yeast. Other mitochondrial protein URPs were also increased, including in the 2-oxodicarboxylate transporter Odc2p, protein import chaperone Ssc1p, and mitochondrial resident protein Cbr1p (Fig. 5B).

Functional Validation of Processes in hpm1 Knockout That Showed Altered Intraprotein or Interprotein Crosslinks

Having found associations, aforementioned, of changed protein and cross-link abundance with some *hpm1* knockout phenotypes, we asked whether we could predict and then functionally validate further *hpm1* knockout phenotypes solely from changes in intraprotein or interprotein crosslinks. Here, we provide three examples, first through considering crosslinks for a single protein, then by considering crosslinks in a large protein complex, and then through considering changes in a eukaryotic organelle.

Pma1p is a plasma membrane proton pump whose role is to directly regulate and acidify the extracellular pH, often in response to environmental and nutrient cues. This is done as a function of its structure (61). Interestingly, many crosslinks within Pma1p were found to be significantly increased in the *hpm1* deletion strain (Fig. 5, *A* and *B* and supplemental Table S6), raising the prospect that it has an altered structure and function. To test whether the rate of media acidification differed between WT and $\Delta hpm1$ strains, we measured media pH as a function of absorbance during exponential growth (Fig. 6A). $\Delta hpm1$ cells exhibited a significantly slower acidification rate compared with the WT strain during its growth ($p < 0.0001$, comparing one-phase decay nonlinear regressions using an extra-sum-of-squares F test). Our crosslinking experiments were performed in cells harvested at midlog growth, a time where changes in media pH of strains were becoming evident. The changes in Pma1p cross-link abundances on *hpm1* deletion (Fig. 5, *A* and *B* and supplemental Table S6), likely associated with a change in protein structure, could here predict a phenotype—being a difference in the rate of media acidification.

Hpm1p is a methyltransferase that methylates H243 of ribosomal protein Rpl3p. Many of the significantly changing URPs did involve ribosomal proteins, with the knockout of *hpm1* resulting in a downregulation of these crosslinks (Fig. 5, *A* and *B* and supplemental Table S6). When ribosomal URPs successfully quantified in both replicates were mapped to the
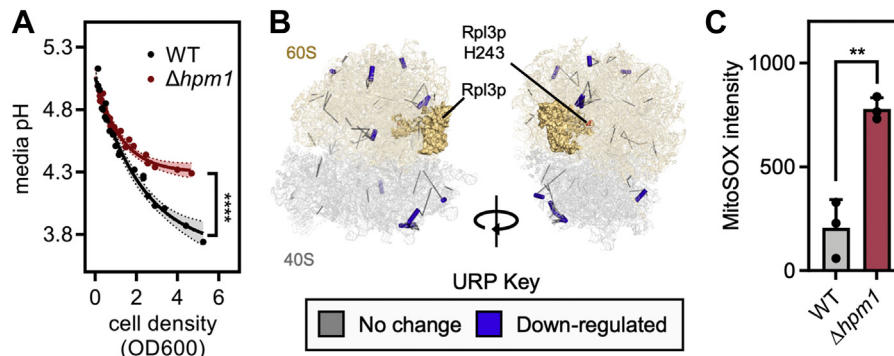

FIG. 6. Changes in intraprotein and interprotein crosslinks can explain or predict cellular phenotypes. *A*, the media pH and absorbance at 600 nm of WT and $\Delta hpm1$ strains grown in SC media were monitored over time to assess the rate of media acidification. This phenotype is affected by Pma1p. Statistical significance reflects the results of comparing nonlinear regression models using an extra-sum-of-squares F test, where **** = $p < 0.0001$, and shading indicates the 95% confidence interval of each model. *B*, mapping of URPs onto a cryo-EM structure of the yeast ribosome in complex with mRNA, tRNA, and eukaryotic elongation factor 2 (eEF2) (PDB: 6GQV). Only crosslinks that were quantified in both replicates are shown, with blue crosslinks determined to be significantly downregulated upon *hpm1* knockout and independent of changes to the underlying protein levels. *C*, to assay for changes to mitochondrial activity and dysfunction, the mean intensity of MitoSOX staining per cell was determined by flow cytometry analysis of 10,000 events in WT and $\Delta hpm1$ cells. The mean population intensity for each replicate was normalized against the matched unlabeled control sample. Statistical analysis was performed using an unpaired two-tailed t test where ** = $p < 0.01$. PDB, Protein Data Bank; SC, synthetic complete; URP, unique residue pair.

cryo-EM structure of the yeast ribosome complexed with mRNA, tRNA, and eukaryotic elongation factor 2 (PDB: 6GQV) (55) (Fig. 6*B*), we found some URPs proximal to Rpl3p with significant change. There was also evidence of some allosteric changes further from Rpl3p, in the 40S subunit. The evaluation of these findings, alone, would suggest changes to ribosome function. Perhaps unsurprisingly, and as noted earlier in this article, the literature shows that *hpm1* deletion leads to increased stop-codon readthrough, programmed −1 ribosomal frameshifting, amino acid misincorporation, and increased resistance to ribosome binding drugs such as cycloheximide and anisomycin (11, 15–17).

Finally, we asked whether crosslinks that change in an organelle's proteins could provide clues to altered function of that organelle. Crosslinks within proteins involved in mitochondrial processes were significantly altered on *hpm1* knockout (discussed in detail in the aforementioned section) (Fig. 5, *A* and *B*). An increased burden of mitochondrial activity/dysfunction results in an increased production of superoxide by the organelle, for example, in respiratory growth when cells require larger and remodeled mitochondria and the ability to perform oxidative phosphorylation (62). To determine whether altered mitochondrial PPIs and structures reflected a change in mitochondrial function, we determined whether the degree of superoxide production differed between WT and *hpm1* deletion strains (Fig. 6*C*). Flow cytometry analysis of cells stained with the mitochondria-specific superoxide sensor MitoSOX revealed a significantly higher degree of staining, and hence higher burden of mitochondrial stress, in *hpm1* deletion cells ($p < 0.01$ resulting from an unpaired two-tailed *t* test). This finding agrees with our crosslinking results of altered mitochondrial processes and in addition may relate to an increased propensity for respiratory growth as suggested by our proteomics data (Fig. 3*C*). More generally, this example shows how changes to multiple protein structures and interactions within an organelle may provide evidence for perturbations to change of function.

DISCUSSION

Hpm1p is the sole histidine methyltransferase in yeast. Previous studies have established the importance of this enzyme for H243$_{Me}$ in Rpl3p and its role in regulating ribosomal assembly and translational fidelity (11, 15–17). Here, we have confirmed the position and stoichiometry of the Rpl3p-catalyzed H243 methyl site. We have also expanded the biology of Hpm1p and histidine methylation by describing new phenotypes for *hpm1* knockout cells. Our observations are consistent with previous systematic screens, which reported ribosomal and nonribosomal phenotypes for such cells (19–30). To investigate the molecular underpinnings of these phenotypes, we used the complementary techniques of proteomics and crosslinking MS. Strikingly, we observed distinct yet functionally convergent changes to many aspects of the proteome including protein abundance, PTMs, structural conformations, and PPIs. From this, we identified a role for Hpm1p in carbon metabolism and membrane biology. Importantly, we found that changes to the interactions or structure of proteins, as detected by crosslinking MS, could explain or predict aspects of Hpm1p biology not seen with expression-based proteomics.

Monitoring Protein Structure and Interactions Generates Novel Insights Into Mechanisms and Phenotypes

A focus of this study was the use of large-scale quantitative crosslinking MS to investigate protein function. Our results highlight several benefits of such an approach, including its orthogonality to protein expression analysis, ability to molecularly explore phenotype in an unbiased manner, and ability to generate mechanistic insights.

An interesting case study is the structure–function changes of Pma1p. Glucose levels can directly regulate its phosphorylation status, its structural conformation and interactions, resulting in modulation of its activity (summarized in Refs. (63, 64)). This plasma membrane ATPase did not change in abundance upon *hpm1* knockout in our deep proteome analysis (Fig. 3). However, changes in Pma1p crosslinks (Fig. 5*B*) on *hpm1* knockout were observed; all were intraprotein crosslinks, capturing changes to the structural conformation of the protein. The discovery of these changes prompted a functional investigation into extracellular pH, which is affected by the proton pumping of Pma1p. Experiments revealed a measurable difference in phenotype, with a lower extracellular acidification rate in Δ*hpm1* (Fig. 6*A*). Given our observation that *hpm1* knockout cells are sensitive to the membrane stressor amphotericin B (Fig. 2), and that changes to pH are known to modulate membrane fidelity (65), altered Pma1p structure may be a mechanism contributing to this phenotype.

The discovery, by crosslinking (Fig. 5, *A* and *B*), of changes in a PPI between two mitochondrial proteins led to a hypothesis of altered mitochondrial activity. Phb1p and Phb2p interact to form the PHB complex; an essential protein scaffold hub that coordinates proteostasis, membrane organization, chaperoning, and the assembly and stabilization of oxidative phosphorylation complexes (reviewed in Ref. (66)). To determine whether this changed interaction affects mitochondrial activity, we used flow cytometry and functional dyes. This detected an increase in mitochondrial superoxide (Fig. 6*C*) in the *hpm1* knockout, which is a byproduct of a high mitochondrial activity and load (reviewed in Ref. (67)). Interestingly, this may explain the high sensitivity of Δ*hpm1* to oxidative stress (Fig. 2). The changes seen to mitochondrial PPIs, and structures of Phb1p, Phb2p, Odc2p, and Ssc1p, may reflect a reorganization of mitochondrial membranes, which is known to occur upon a shift to respiratory growth (62). To summarize this example, we were able to detect and

validate a functional effect, indicated by a change in PPI, and which was detected by crosslinking MS.

Alterations to Carbon Metabolism and Membranes in Δhpm1 Cells

In the *hpm1* knockout, there was evidence for the modulation of sugar synthesis and metabolism. Our proteomic expression analysis revealed that some enzymes involved in glucose metabolism and fermentative growth were specifically downregulated in Δ*hpm1* compared with WT (Fig. 3). These changes may reflect a metabolic priming toward respiratory growth, also evidenced by the fact that Δ*hpm1* cells have a decreased growth rate on glucose but an increased growth rate on alternative carbon sources, such as ethanol (19), xylose (25), glycerol (19), and sucrose or fructose (19). Notably, the protein Ygp1p, which was significantly downregulated in Δ*hpm1*, is involved in physical and behavioral changes associated with nutrient sensing. Specifically, Ygp1p is implicated in the regulation of biofilm formation and is itself regulated by extracellular glucose levels (68, 69). We did not detect a concomitant increase in respiratory proteins. However, in our study, cells were cultured in media containing glucose as the sole carbon source. They were harvested at midlog phase, before high levels of ethanol could accumulate from fermentation (the diauxic shift) and before substantial metabolic remodeling occurs. We did however directly observe alterations to the structure of two enzymes involved in gluconeogenesis and glycolysis, Cdc19p and Eno2p, in our crosslinking data (Fig. 5B).

We found that the trehalose biosynthetic pathway (Tsl1p, Tps1p, Tps2p, and Tps3p) was downregulated upon *hpm1* knockout (Fig. 3, C and D). The disaccharide trehalose is up to 15% of the dry cell weight of yeast (70) and acts not only as a carbohydrate reservoir but also as a structural protectant against physical stressors such as freezing and drying (reviewed in Refs. (70, 71)). The downregulation of the trehalose pathway is consistent with our observations that Δ*hpm1* yeasts are sensitive to cold stress (Fig. 2) and the observations by others of a decreased tolerance to desiccation (26). Interestingly, the trehalose precursor trehalose-6-phosphate, which is catalyzed by Tps1p from glucose-6-phosphate and UDP-glucose, has also been shown to directly regulate the ability of yeast to undergo glycolysis (72, 73), and Δ*tps1* cells entirely lose the ability to grow on glucose (73).

We found that the deletion of *hpm1* resulted in alterations to membrane integrity and function. Our plate assays identified severe growth defects in the membrane stressor 0.1 μg/ml amphotericin-B upon *hpm1* knockout (Fig. 2), and our crosslinking and follow-up validation studies revealed a change to Pma1p structure and function (Figs. 5B and 6A). There are several other molecular links to membrane dysfunction in our study. Amphotericin-B sequesters ergosterol (74), which is important for the structure and function of membranes, and to membrane-bound organelles including

vacuoles. Indeed, *hpm1* knockouts are reported to have alterations to both vacuolar structure and function (27, 75), which may be associated with our observed change in the abundance of the vacuolar protein Pho84p, which was highly downregulated in the knockout strain. Dysfunctions in sterol processes are known to result in a decreased tolerance to salt stress (76), and we found that Δ*hpm1* yeast also exhibited significant growth defects under 1 M NaCl. Alternatively, the salt stress phenotype could be related to the changes in the intralink URP we observed in the Ena2p sodium transporter protein. We were also able to identify likely changes in structure within other membrane proteins (which were not changing in abundance themselves) associated with Δ*hpm1* phenotypes. These proteins included the plasma membrane ATPase Pma1p (as noted previously), the endoplasmic reticulum protein importer Kar2p, and mitochondrial membrane protein sorters Phb1p and Phb2p.

The Substrates and Function of Hpm1p

In addition to revealing new biology for Hpm1p, our study has also generated insights into the direct function of Hpm1p. These include the possibility of undescribed substrates for the enzyme. The question of substrate proteins for Hpm1p, that exist in addition to Rpl3p, remains unresolved. In one study (15), radiolabeled methylhistidines were detected by amino acid analysis and largely attributed to ribosomal fractions. A small amount of radiolabel was however detected in membrane-bound organelles. This was attributed to the process of ribosome biogenesis within the nucleus, as SDS-PAGE revealed only one band, corresponding to Rpl3p in size, that was absent in Δ*hpm1* fractions (15). A later study by the same group (16) constructed an Rpl3p H243A mutant to detect radiolabeled methylation in potential non-Rpl3p substrates. This revealed two potential substrates in the postmitochondrial cellular fraction, although their identities were not determined (16). While we did not find any evidence for alternative Hpm1p substrates in our reanalysis of published methyl-SILAC–LC–MS/MS data (38), novel methyl-histidine sites could be either entirely absent or present at low stoichiometry in the growth conditions sampled. Equally, they could only be amenable to discovery with different endoproteinases to those used (38). Our investigation of the H243A mutant (supplemental Fig. S2) revealed some evidence for additional Hmp1p substrates, in that the mutant does not completely phenocopy the *hmp1* knockout. This phenomenon was also seen previously (16). But the possibility also remains that Hpm1p protein itself has additional molecular functions to histidine methyltransferase activity. Interestingly, the stressors that just affected Δ*hpm1* but not Rpl3p H243A (oxidative stress, amphotericin B) related to the mitochondrial and membrane processes that we could functionally validate.

Another means by which Hpm1p may directly mediate phenotypes, that we and others have observed, is through the modulation of ribosome heterogeneity. Alterations to the

ribosome's protein/RNA composition, PTM, and subcellular localization have been demonstrated to modulate translational specificity and fidelity (reviewed in Ref. (77)). Our study, and those of others (11, 15–17) have only studied Rpl3p H243 methyl site stoichiometry in cells grown in media containing glucose as the sole carbon source. In these conditions, the site appears to be constitutively present. However, in another link to metabolism, it is known that the levels of *hpm1* transcripts are regulated by metabolic conditions; for example, they are specifically downregulated in response to xylose (25). As the H243 site lies within the decoding center of the ribosome, and makes direct contact with rRNAs, modulation of Rpl3p histidine methylation has potential to allosterically alter the structure of this complex, and thus alter translational specificity. In fact, modulation of translation specificity through Rpl3p histidine methylation has been observed in the knockout of *hpm1*'s human ortholog *METTL18*, which displays altered ribosome occupancies for specific groups of genes, including those involving vacuolar and metabolic processes (12). It has also been shown to affect ribosomal translocation at tyrosine residues (78). There is some functional evidence of change to the structure of the ribosome in *hpm1* knockout cells, which display increased resistance to translational inhibitors such as cycloheximide, verrucarin, and anisomycin (11, 15–17). In our study, we were able to directly observe specific changes to the structure of some ribosomal proteins, both locally surrounding Rpl3p and distally (Fig. 6*B*). These allosteric changes were expected as the H243 residue makes direct contact with the rRNA core of the assembled ribosome.

CONCLUSIONS

Our study has shown how untargeted screens of PPIs and low-resolution measures of protein structure, combined with functional readouts and traditional quantitative proteomics, can shed new light on complicated phenotypes. It has substantially expanded the biological role of histidine methylation in *S. cerevisiae* and raised the possibility of alternative Hmp1p substrates. This study has also raised interesting questions about the role of histidine methylation as a possible modulator of ribosomal heterogeneity and how it may alter translational specificity. Technical advances, such as the development of histidine methylation affinity reagents and the use of orthogonal proteomics methods, will ultimately decipher the enigmatic functions of Hpm1p.

DATA AVAILABILITY

All MS data and spectral identifications have been deposited in the ProteomeXchange Consortium *via* the PRIDE partner repository (79) with the dataset identifier PXD027953. Annotated spectra showing the best CSM for each cross-linked peptide pair has been provided as supplemental data (supplemental Fig. S6). Targeted MS analyses have been

uploaded to Panorama, available at https://panoramaweb.org/0M3Z0c.url. HTML RMarkdown reports and R scripts are available for the crosslinking analyses, accessible at https://github.com/TaraBartolec/Hpm1.

Supplemental data—This article contains supplemental data.

Conflict of interest—The authors declare no competing interests.

Abbreviations—The abbreviations used are: BDP–NHP, biotin–aspartate proline–*N*-hydroxyphthalimide; BL, Boca and Leek's FDR regression method; CSM, cross-link spectral match; FDR, false discovery rate; GO, Gene Ontology; H243, histidine 243; H243Me, methylation of H243; HCD, higher-energy collision dissociation; Hpm1p, histidine protein methyltransferase 1; IAA, iodoacetamide; MS, mass spectrometry; NCE, normalized collision energy; PDB, Protein Data Bank; PIR, protein interaction reporter; PPI, protein–protein interaction; PTM, post-translational modification; RT, room temperature; SC, synthetic complete; SCX, strong cation exchange;

SILAC, stable isotope labeling of amino acids in cell culture; UNSW, University of New South Wales; URP, unique residue pair.

REFERENCES

1. Kwiatkowski, S., and Drozak, J. (2020) Protein histidine methylation. *Curr. Protein Pept. Sci.* **21**, 675–689
2. Jakobsson, M. E. (2021) Enzymology and significance of protein histidine methylation. *J. Biol. Chem.* **297**, 101130
3. Lv, M., Cao, D., Zhang, L., Hu, C., Li, S., Zhang, P., Zhu, L., Yi, X., Li, C., Yang, A., Yang, Z., Zhu, Y., Zhang, K., and Pan, W. (2021) METTL9 mediated N1-histidine methylation of zinc transporters is required for tumor growth. *Protein Cell* **12**, 965–970
4. Davydova, E., Shimazu, T., Schuhmacher, M. K., Jakobsson, M. E., Willemen, H. L. D. M., Liu, T., Moen, A., Ho, A. Y. Y., Małecki, J., Schroer, L., Pinto, R., Suzuki, T., Grønsberg, I. A., Sohtome, Y., Akakabe, M., *et al*. (2021) The methyltransferase METTL9 mediates pervasive 1-methylhistidine modification in mammalian proteomes. *Nat. Commun.* **12**, 891
5. Kwiatkowski, S., Seliga, A. K., Vertommen, D., Terreri, M., Ishikawa, T., Grabowska, I., Tiebe, M., Teleman, A. A., Jagielski, A. K., Veiga-Da-Cunha, M., and Drozak, J. (2018) SETD3 protein is the actin-specific histidine N-methyltransferase. *eLife* **7**, e37921
6. Wilkinson, A. W., Diep, J., Dai, S., Liu, S., Ooi, Y. S., Song, D., Li, T. M., Horton, J. R., Zhang, X., Liu, C., Trivedi, D.v., Ruppel, K. M., Vilches-Moure, J. G., Casey, K. M., Mak, J., *et al*. (2019) SETD3 is an actin histidine methyltransferase that prevents primary dystocia. *Nature* **565**, 372–376
7. Diep, J., Ooi, Y. S., Wilkinson, A. W., Peters, C. E., Foy, E., Johnson, J. R., Zengel, J., Ding, S., Weng, K. F., Laufman, O., Jang, G., Xu, J., Young, T., Verschueren, E., Kobluk, K. J., *et al*. (2019) Enterovirus pathogenesis requires the host methyltransferase SETD3. *Nat. Microbiol.* **4**, 2523–2537
8. Cheng, X., Hao, Y., Shu, W., Zhao, M., Zhao, C., Wu, Y., Peng, X., Yao, P., Xiao, D., Qing, G., Pan, Z., Yin, L., Hu, D., and Du, H. N. (2017) Cell cycle-dependent degradation of the methyltransferase SETD3 attenuates cell proliferation and liver tumorigenesis. *J. Biol. Chem.* **292**, 9022–9033
9. Chen, Z., Yan, C. T., Dou, Y., Viboolsittiseri, S. S., and Wang, J. H. (2013) The role of a newly identified SET domain-containing protein, SETD3, in oncogenesis. *Haematologica* **98**, 739–743
10. Kapell, S., and Jakobsson, M. E. (2021) Large-scale identification of protein histidine methylation in human cells. *NAR Genom. Bioinform.* **3**. https://doi.org/10.1093/nargab/lqab045
11. Webb, K. J., Zurita-Lopez, C. I., Al-Hadid, Q., Laganowsky, A., Young, B. D., Lipson, R. S., Souda, P., Faull, K. F., Whitelegge, J. P., and Clarke, S. G. (2010) A novel 3-methylhistidine modification of yeast ribosomal protein Rpl3 is dependent upon the YIL110W methyltransferase. *J. Biol. Chem.* **285**, 37598–375606
12. Małecki, J. M., Odonohue, M. F., Kim, Y., Jakobsson, M. E., Gessa, L., Pinto, R., Wu, J., Davydova, E., Moen, A., Olsen, J.v., Thiede, B., Gleizes, P. E., Leidel, S. A., and Falnes, P. (2021) Human METTL18 is a histidine-specific methyltransferase that targets RPL3 and affects ribosome biogenesis and function. *Nucl. Acids Res.* **49**, 3185–3203
13. Meskauskas, A., and Dinman, J. D. (2008) Ribosomal protein L3 functions as a "rocker switch" to aid in coordinating of large subunit-associated functions in eukaryotes and Archaea. *Nucl. Acids Res.* **36**, 6175–6186
14. Meskauskas, A., and Dinman, J. D. (2007) Ribosomal protein L3: Gate-keeper to the A site. *Mol. Cell* **25**, 878–888
15. Al-Hadid, Q., Roy, K., Munroe, W., Dzialo, M. C., Chanfreau, G. F., and Clarke, S. G. (2014) Histidine methylation of yeast ribosomal protein Rpl3p is required for proper 60S subunit assembly. *Mol. Cel. Biol.* **34**, 2903–2916
16. Al-Hadid, Q., Roy, K., Chanfreau, G., and Clarke, S. G. (2016) Methylation of yeast ribosomal protein Rpl3 promotes translational elongation fidelity. *RNA* **22**, 489–498
17. Al-Hadid, Q., White, J., and Clarke, S. (2016) Ribosomal protein methyl-transferases in the yeast Saccharomyces cerevisiae: Roles in ribosome biogenesis and translation. *Biochem. Biophys. Res. Commun.* **470**, 552–557
18. Cherry, J. M., Hong, E. L., Amundsen, C., Balakrishnan, R., Binkley, G., Chan, E. T., Christie, K. R., Costanzo, M. C., Dwight, S. S., Engel, S. R., Fisk, D. G., Hirschman, J. E., Hitz, B. C., Karra, K., Krieger, C. J., *et al*. (2012) Saccharomyces genome database: The genomics resource of budding yeast. *Nucl. Acids Res.* **40**, D700–D705
19. Qian, W., Ma, D., Xiao, C., Wang, Z., and Zhang, J. (2012) The genomic landscape and evolutionary resolution of antagonistic pleiotropy in yeast. *Cell Rep.* **2**, 1399–1410
20. Steinmetz, L. M., Scharfe, C., Deutschbauer, A. M., Mokranjac, D., Herman, Z. S., Jones, T., Chu, A. M., Giaever, G., Prokisch, H., Oefner, P. J., and Davis, R. W. (2002) Systematic screen for human disease genes in yeast. *Nat. Genet.* **31**, 400–404
21. Breslow, D. K., Cameron, D. M., Collins, S. R., Schuldiner, M., Stewart-Ornstein, J., Newman, H. W., Braun, S., Madhani, H. D., Krogan, N. J., and Weissman, J. S. (2008) A comprehensive strategy enabling high-resolution functional analysis of the yeast genome. *Nat. Met.* **5**, 711–718
22. Brown, J. A., Sherlock, G., Myers, C. L., Burrows, N. M., Deng, C., Wu, H. I., McCann, K. E., Troyanskaya, O. G., and Brown, J. M. (2006) Global analysis of gene function in yeast by quantitative phenotypic profiling. *Mol. Syst. Biol.* **2**. https://doi.org/10.1038/msb4100043
23. Deutschbauer, A. M., Jaramillo, D. F., Proctor, M., Kumm, J., Hillenmeyer, M. E., Davis, R. W., Nislow, C., and Giaever, G. (2005) Mechanisms of haploinsufficiency revealed by genome-wide profiling in yeast. *Genetics* **169**, 1915–1925
24. Jorgensen, P., Nishikawa, J. L., Breitkreutz, B. J., and Tyers, M. (2002) Systematic identification of pathways that couple cell growth and division in yeast. *Science* **297**, 395–400
25. Bengtsson, O., Jeppsson, M., Sonderegger, M., Parachin, N. S., Sauer, U., Hahn-Hägerdal, B., and Gorwa-Grauslund, M. F. (2008) Identification of common traits in improved xylose-growing Saccharomyces cerevisiae for inverse metabolic engineering. *Yeast* **25**, 835–847
26. Ratnakumar, S., Hesketh, A., Gkargkas, K., Wilson, M., Rash, B. M., Hayes, A., Tunnacliffe, A., and Oliver, S. G. (2011) Phenomic and transcriptomic analyses reveal that autophagy plays a major role in desiccation tolerance in Saccharomyces cerevisiae. *Mol. BioSyst.* **7**, 139–149
27. Michaillat, L., and Mayer, A. (2013) Identification of genes affecting vacuole membrane fragmentation in Saccharomyces cerevisiae. *PLoS One* **8**, e54160
28. Lesage, G., Sdicu, A. M., Ménard, P., Shapiro, J., Hussein, S., and Bussey, H. (2004) Analysis of β-1,3-glucan assembly in Saccharomyces cerevisiae using a synthetic interaction network and altered sensitivity to caspo-fungin. *Genetics* **167**, 35–49
29. Lesage, G., Shapiro, J., Specht, C. A., Sdicu, A. M., Ménard, P., Hussein, S., Tong, A. H. Y., Boone, C., and Bussey, H. (2005) An interactional network of genes involved in chitin synthesis in Saccharomyces cerevisiae. *BMC Genet.* **6**, 8
30. Tong, A. H. Y., Lesage, G., Bader, G. D., Ding, H., Xu, H., Xin, X., Young, J., Berriz, G. F., Brost, R. L., Chang, M., Chen, Y. Q., Cheng, X., Chua, G., Friesen, H., Goldberg, D. S., *et al*. (2004) Global mapping of the yeast genetic interaction network. *Science* **303**, 808–813
31. Chavez, J. D., Mohr, J. P., Mathay, M., Zhong, X., Keller, A., and Bruce, J. E. (2019) Systems structural biology measurements by *in vivo* cross-linking with mass spectrometry. *Nat. Protoc.* **14**, 2318–2343
32. Winzeler, E. A., Shoemaker, D. D., Astromoff, A., Liang, H., Anderson, K., Andre, B., Bangham, R., Benito, R., Boeke, J. D., Bussey, H., Chu, A. M., Connelly, C., Davis, K., Dietrich, F., Dow, S. W., *et al*. (1999) Functional characterization of the S. cerevisiae genome by gene deletion and parallel analysis. *Science* **285**, 901–906
33. Janke, C., Magiera, M. M., Rathfelder, N., Taxis, C., Reber, S., Maekawa, H., Moreno-Borchart, A., Doenges, G., Schwob, E., Schiebel, E., and Knop, M. (2004) A versatile toolbox for PCR-based tagging of yeast genes: New fluorescent proteins, more markers and promoter substitution cassettes. *Yeast* **21**, 947–962
34. Gietz, R. D., and Schiestl, R. H. (2007) High-efficiency yeast transformation using the LiAc/SS carrier DNA/PEG method. *Nat. Protoc.* **2**, 31–34
35. Hamey, J. J., Winter, D. L., Yagoub, D., Overall, C. M., Hart-Smith, G., and Wilkins, M. R. (2016) Novel N-terminal and lysine methyltransferases that target translation elongation factor 1A in yeast and human. *Mol. Cell Proteomics* **15**, 164–176

36. Separovich, R. J., Wong, M. W. M., Chapman, T. R., Slavich, E., Hamey, J. J., and Wilkins, M. R. (2021) Post-translational modification analysis of Saccharomyces cerevisiae histone methylation enzymes reveals phosphorylation sites of regulatory potential. _J. Biol. Chem._ **296**, 100192

37. Pino, L. K., Searle, B. C., Bollinger, J. G., Nunn, B., MacLean, B., and MacCoss, M. J. (2020) The Skyline ecosystem: Informatics for quantitative mass spectrometry proteomics. _Mass Spectrom. Rev._ **39**, 229–244

38. Hart-Smith, G., Yagoub, D., Tay, A. P., Pickford, R., and Wilkins, M. R. (2016) Large scale mass spectrometry-based identifications of enzyme-mediated protein methylation are subject to high false discovery rates. _Mol. Cell Proteomics_ **15**, 989–1006

39. Tay, A. P., Geoghegan, V., Yagoub, D., Wilkins, M. R., and Hart-Smith, G. (2018) MethylQuant: a tool for sensitive validation of enzyme-mediated protein methylation sites from heavy-methyl SILAC data. _J. Proteome Res._ **17**, 359–373

40. Dannenmaier, S., Stiller, S. B., Morgenstern, M., Lübbert, P., Oeljeklaus, S., Wiedemann, N., and Warscheid, B. (2018) Complete native stable isotope labeling by amino acids of Saccharomyces cerevisiae for global proteomic analysis. _Anal. Chem._ **90**, 10501–10509

41. Tyanova, S., Temu, T., and Cox, J. (2016) The MaxQuant computational platform for mass spectrometry-based shotgun proteomics. _Nat. Protoc._ **11**, 2301–2319

42. Theodorakis, E., Antonakis, A. N., Baltsavia, I., Pavlopoulos, G. A., Samiotaki, M., Amoutzias, G. D., _et al_. (2021) ProteoSign v2: A faster and evolved user-friendly online tool for statistical analyses of differential proteomics. _Nucl. Acids Res._ **49**, W573–W577

43. Mi, H., Muruganujan, A., and Thomas, P. D. (2013) PANTHER in 2013: Modeling the evolution of gene function, and other gene attributes, in the context of phylogenetic trees. _Nucl. Acids Res._ **41**, D377–D386

44. Kessner, D., Chambers, M., Burke, R., Agus, D., and Mallick, P. (2008) ProteoWizard: Open source software for rapid proteomics tools development. _Bioinformatics_ **24**, 2534–2536

45. Mohr, J. P., Perumalla, P., Chavez, J. D., Eng, J. K., and Bruce, J. E. (2018) Mango: A general tool for collision induced dissociation-cleavable cross-linked peptide identification. _Anal. Chem._ **90**, 6028–6034

46. Eng, J. K., Jahan, T. A., and Hoopmann, M. R. (2013) Comet: An open-source MS/MS sequence database search tool. _Proteomics_ **13**, 22–24

47. Keller, A., Chavez, J. D., and Bruce, J. E. (2019) Increased sensitivity with automated validation of XL-MS cleavable peptide cross-links. _Bioinformatics_ **35**, 895–897

48. Schweppe, D. K., Zheng, C., Chavez, J. D., Navare, A. T., Wu, X., Eng, J. K., and Bruce, J. E. (2016) XLinkDB 2.0: Integrated, large-scale structural analysis of protein cross-linking data. _Bioinformatics_ **32**, 2716–2718

49. Berman, H. M., Westbrook, J., Feng, Z., Gilliland, G., Bhat, T. N., Weissig, H., Shindyalov, I. N., and Bourne, P. E. (2000) The protein data bank. _Nucl. Acids Res._ **28**, 235–242

50. Kahraman, A., Malmström, L., and Aebersold, R. (2011) Xwalk: Computing and visualizing distances in cross-linking experiments. _Bioinformatics_ **27**, 2163–2164

51. Dana, J. M., Gutmanas, A., Tyagi, N., Qi, G., O'Donovan, C., Martin, M., and Velankar, S. (2019) SIFTS: Updated Structure integration with function, taxonomy and sequences resource allows 40-fold increase in coverage of structure-based annotations for proteins. _Nucl. Acids Res._ **47**, D482–D489

52. Boca, S. M., and Leek, J. T. (2018) A direct approach to estimating false discovery rates conditional on covariates. _PeerJ_ **6**, e6035

53. Shannon, P., Markiel, A., Ozier, O., Baliga, N. S., Wang, J. T., Ramage, D., Amin, N., Schwikowski, B., and Ideker, T. (2003) Cytoscape: A software environment for integrated models of biomolecular interaction networks. _Genome Res._ **13**, 2498–2504

54. Schiffrin, B., Radford, S. E., Brockwell, D. J., and Calabrese, A. N. (2020) PyXlinkViewer: A flexible tool for visualization of protein chemical cross-linking data within the PyMOL molecular graphics system. _Protein Sci._ **29**, 1851–1857

55. Pellegrino, S., Demeshkina, N., Mancera-Martinez, E., Melnikov, S., Simonetti, A., Myasnikov, A., Yusupov, M., Yusupova, G., and Hashem, Y. (2018) Structural insights into the role of diphthamide on elongation factor 2 in mRNA reading-frame maintenance. _J. Mol. Biol._ **430**, 2677–2687

56. Ong, S. E., Mittler, G., and Mann, M. (2004) Identifying and quantifying _in vivo_ methylation sites by heavy methyl SILAC. _Nat. Met._ **1**, 119–126

57. Alonso-López, Di., Campos-Laborie, F. J., Gutiérrez, M. A., Lambourne, L., Calderwood, M. A., Vidal, M., and de Las Rivas, J. (2019) _APID Database: Redefining Protein-Protein Interaction Experimental Evidences and Binary Interactomes_. Database, Oxford. 2019

58. Dai, H., and Wang, Z. (2014) Histone modification patterns and their responses to environment. _Curr. Environ. Health Rep._ **1**, 11–21

59. Rando, O. J., and Winston, F. (2012) Chromatin and transcription in yeast. _Genetics_ **190**, 351–387

60. Signorile, A., Sgaramella, G., Bellomo, F., and de Rasmo, D. (2019) Prohibitins: A critical role in mitochondrial functions and implication in diseases. _Cells_ **8**, 71

61. Portillo, F. (2000) Regulation of plasma membrane H+-ATPase in fungi and plants. _Biochim. Biophys. Acta - Rev. Biomem._ **1469**, 31–42

62. di Bartolomeo, F., Malina, C., Campbell, K., Mormino, M., Fuchs, J., Vorontsov, E., Gustafsson, C. M., and Nielsen, J. (2020) Absolute yeast mitochondrial proteome quantification reveals trade-off between biosynthesis and energy generation during diauxic shift. _Proc. Natl. Acad. Sci. U. S. A._ **117**, 7524–7535

63. Morsomme, P., Slayman, C. W., and Goffeau, A. (2000) Mutagenic study of the structure, function and biogenesis of the yeast plasma membrane H+-ATPase. _Biochim. Biophys. Acta - Rev. Biomem._ **1469**, 133–157

64. Lecchi, S., Nelson, C. J., Allen, K. E., Swaney, D. L., Thompson, K. L., Coon, J. J., Sussman, M. R., and Slayman, C. W. (2007) Tandem phosphorylation of Ser-911 and Thr-912 at the C terminus of yeast plasma membrane H+-ATPase leads to glucose-dependent activation. _J. Biol. Chem._ **282**, 35471–35481

65. Brandão, R. L., Rosa, J. C. C., Nicoli, J. R., Almeida, M. V. S., do Carmo, A. P., Queiros, H. T., and Castro, I. M. (2014) Investigating acid stress response in different Saccharomyces strains. _J. Mycol._ **2014**, 1–9

66. Artal-Sanz, M., and Tavernarakis, N. (2009) Prohibitin and mitochondrial biology. _Trends Endocrinol. Metab._ **20**, 394–401

67. Kitagaki, H., and Takagi, H. (2014) Mitochondrial metabolism and stress response of yeast: Applications in fermentation technologies. _J. Biosci. Bioeng._ **117**, 383–393

68. Vandenbosch, D., de Canck, E., Dhondt, I., Rigole, P., Nelis, H. J., and Coenye, T. (2013) Genomewide screening for genes involved in biofilm formation and miconazole susceptibility in Saccharomyces cerevisiae. _FEMS Yeast Res._ **13**, 720–730

69. Destruelle, M., Holzer, H., and Klionsky, D. J. (1994) Identification and characterization of a novel yeast gene: The YGP1 gene product is a highly glycosylated secreted protein that is synthesized in response to nutrient limitation. _Mol. Cel. Biol._ **14**, 2740–2754

70. Lillie, S. H., and Pringle, J. R. (1980) Reserve carbohydrate metabolism in Saccharomyces cerevisiae: Responses to nutrient limitation. _J. Bacteriol._ **143**, 1384–1394

71. Eleutherio, E., Panek, A., de Mesquita, J. F., Trevisol, E., and Magalhães, R. (2015) Revisiting yeast trehalose metabolism. _Curr. Genet._ **61**, 263–274

72. Vicente, R. L., Spina, L., Gómez, J. P. L., Dejean, S., Parrou, J. L., and François, J. M. (2018) Trehalose-6-phosphate promotes fermentation and glucose repression in Saccharomyces cerevisiae. _Microb. Cell_ **5**, 444–459

73. Thevelein, J. M., and Hohmann, S. (1995) Trehalose synthase: Guard to the gate of glycolysis in yeast? _Trends Biochem. Sci._ **20**, 3–10

74. Gray, K. C., Palacios, D. S., Dailey, I., Endo, M. M., Uno, B. E., Wilcock, B. C., and Burke, M. D. (2012) Amphotericin primarily kills yeast by simply binding ergosterol. _Proc. Natl. Acad. Sci. U. S. A._ **109**, 2234–2239

75. Bonangelino, C. J., Chavez, E. M., and Bonifacino, J. S. (2002) Genomic screen for vacuolar protein sorting genes in Saccharomyces cerevisiae. _Mol. Biol. Cell_ **13**, 2486–2501

76. Kodedová, M., and Sychrová, H. (2015) Changes in the sterol composition of the plasma membrane affect membrane potential, salt tolerance and the activity of multidrug resistance pumps in Saccharomyces cerevisiae. _PLoS One_ **10**, e0139306

77. Emmott, E., Jovanovic, M., and Slavov, N. (2019) Ribosome stoichiometry: From form to function. _Trends Biochem. Sci._ **44**, 95–109

78. Matsuura-Suzuki, E., Shimazu, T., Takahashi, M., Kotoshiba, K., Suzuki, T., Kashiwagi, K., Sohtome, Y., Akakabe, M., Sodeoka, M., Dohmae, N., Ito, T., Shinkai, Y., and Iwasaki, S. (2022) METTL18-mediated histidine methylation on RPL3 modulates translation elongation for proteostasis maintenance. _Elife_ **11**, e72780

79. Perez-Riverol, Y., Bai, J., Bandla, C., García-Seisdedos, D., Hewapathirana, S., Kamatchinathan, S., Kundu, D. J., Prakash, A., Frericks-Zipper, A., Eisenacher, M., Walzer, M., Wang, S., Brazma, A., and Vizcaíno, J. A. (2022) The PRIDE database resources in 2022: a hub for mass spectrometry-based proteomics evidences. _Nucleic Acids Res_ **50**, D543–D552